RSC Advances

PAPER

View Article Online
View Journal | View Issue

Cite this: *RSC Adv.*, 2025, **15**, 50810

Novel thiazole–phthalimide-based heterobimetallic Cu(II)–M(II) complexes: synthesis, characterization, and therapeutic properties against arsenic-induced lung damage in rats

Naglaa A. Ali,[a] Ghada H. Elsayed, *[ab] Asmaa M. Fahim, *[c] Mariam G. Rizk[d] and Nelly H. Mahmoud[d]

Prolonged exposure to arsenic trioxide (As_2O_3) brings about oxidative stress, inflammation, apoptosis, and, ultimately, irreversible pulmonary damage. In this study, we synthesized and characterized a new series of thiazole–phthalimide-based heterobimetallic Cu(II)–M(II)/M(I) complexes (M = Co, Ni, Zn, Ag) using elemental analysis, spectroscopic methods (FT-IR, UV–Vis, ^{1}H NMR, MS), thermal techniques (TGA/DTG), and X-ray diffraction (XRD). We subsequently evaluated the protective effects of these complexes against As_2O_3-induced pulmonary toxicity in female Wistar rats. Chronic As_2O_3-exposure (4 mg kg^{-1} for 30 days) significantly increased oxidative stress markers, including malondialdehyde (MDA), BCL2, and APAF-1, while markedly reducing glutathione (GSH) activity. In addition, As_2O_3-exposure significantly raised the expression levels of apoptotic genes (BAX and ERK) and autophagic genes (Beclin1 and LC3). These findings were supported by the histological examination of lung tissue. Among the analogues produced, As_2O_3-Cu–Zn–PTP and As_2O_3-Cu–Ni–PTP provided robust attenuation of oxidative stress, restored antioxidant defenses, and modulated the expression of apoptotic and autophagic genes. Additional support came from molecular docking and MD simulations, both confirming stable ligand–protein binding with BAX (PDB 4S0O) and BCL-2 (PDB 1G5M). In addition, all interactions were substantiated by favorable MM/PBSA energy profiles.

Received 17th September 2025
Accepted 10th November 2025

DOI: 10.1039/d5ra07055d

rsc.li/rsc-advances

1. Introduction

The design and synthesis of hetero-metallic coordination complexes have garnered significant attention in recent years due to their potential applications in various fields, including catalysis, materials science, and medicinal chemistry.[1–3] These complexes, particularly those incorporating transition metals, offer a unique opportunity to explore synergistic interactions between multiple metal centers, leading to novel properties that are often unattainable with mono-metallic systems.[4,5] Among these, conjugated organic ligands capable of bridging different metal ions have proven especially valuable in constructing architecturally well-defined and functionally diverse assemblies.[6] Their chemical and physical versatility enables applications in molecular electronics, luminescent devices, catalysis, and biological systems,[7,8] including antimicrobial, antiviral, and DNA-interactive agents.[9] Thiazole-based ligands, known for their strong coordination ability through nitrogen and sulfur donor atoms, have emerged as prominent scaffolds in this context. These heterocycles not only enhance the stability and reactivity of metal complexes but also impart distinct biological activities such as antibacterial, antifungal, and anticancer effects.[10] Similarly, phthalimide (isoindoline-1,3-dione) derivatives have demonstrated considerable pharmacological significance, exhibiting antioxidant, anti-inflammatory, and cytotoxic properties.[11,12] When integrated into coordination frameworks, these ligands can form potent metal–drug adducts with enhanced biological activity due to improved cellular uptake and interactions with biomolecular targets.[9,13] Of particular relevance is the therapeutic potential of copper(II) complexes, which exhibit preferential uptake by cancer cells due to their redox activity and membrane permeability. Incorporating a second metal center, such as Zn(II), Ni(II), Co(II), or Ag(I), into a Cu(II)-based complex could further modulate the complex's reactivity and enhance its pharmacological profile. This dual-metal strategy presents a promising avenue for developing next-generation Metallo pharmaceuticals with synergistic biological functions.[14] In parallel, environmental toxicology has

[a]*Hormones Department, Medical and Clinical Studies Institute, National Research Centre, Giza, 12622, Egypt. E-mail: gh.hamdi@nrc.sci.eg; ghadanrc@yahoo.com*
[b]*Stem Cells Lab, Centre of Excellence for Advanced Sciences, National Research Centre, Giza, 12622, Egypt*
[c]*Department of Green Chemistry, National Research Centre, Dokki, Cairo, P. O. 12622, Egypt. E-mail: am.abdel-wahid@nrc.sci.eg; asmaamahmoud8521@gmail.com*
[d]*Chemistry Department, Faculty of Women for Arts, Science and Education, Ain-Shams University, Cairo, 11757, Egypt*

highlighted the urgent need for novel agents to combat the damage caused by heavy metal contaminants such as As_2O_3.[15] As a global environmental toxicant, arsenic exposure, particularly in the form of As_2O_3 is associated with severe oxidative stress, cellular dysfunction, and tissue damage, especially in the lungs. Chronic As_2O_3 ingestion has been implicated in lipid peroxidation, DNA strand breaks, glutathione depletion, and disruption of antioxidant defense systems, leading to respiratory diseases and compromised lung function. These pathological effects are closely tied to oxidative stress, apoptosis, and autophagy dysregulation.[16] Moreover, apoptosis, or programmed cell death, is crucial for maintaining tissue homeostasis by eliminating damaged or unnecessary cells. It involves characteristic changes such as cell shrinkage, membrane blebbing, and DNA fragmentation. The intrinsic pathway is regulated by the BCL2 protein family, where MCL-1 supports survival, while BAX promotes Cytochrome c release, apoptosome formation, and caspase activation leading to cell death.[17] Apoptosis is also linked to signaling cascades such as the MAPK pathway, with ERKs activated by phosphorylation in response to stress and growth signals.[18] Autophagy, a related process, maintains homeostasis by degrading and recycling intracellular components through autophagic flux, which includes autophagosome formation, lysosomal fusion, and degradation. This pathway is coordinated by more than 30 autophagy-related proteins, including PI3K, Beclin1, LC3, ULK1, AMPK, AKT, and P62.[19]

The present study aims to develop and evaluate a series of novel hetero-metallic complexes based on a newly synthesized thiazole-phthalimide ligand, N^1,N^2-bis(4-phenylthiazole-2-yl) phthalimide (**PTP**), with copper(II) as a fixed metal and varying secondary metal centers (Zn(II), Ni(II), Co(II), and Ag(I)). These complexes were characterized using spectroscopic and thermal methods. *In vivo* investigations were performed using an arsenic-induced lung injury rat model to explore the therapeutic potential of the synthesized complexes. The study focused on unraveling the mechanistic pathways involving oxidative stress, apoptosis, and autophagy, providing insights into their possible use as therapeutic agents against heavy metal-induced lung toxicity. Thus, the discovery of new potent agents that are involved in the apoptosis and autophagy processes may offer new opportunities for the treatment of lung diseases. Furthermore, the docking analysis and molecular dynamic simulation of the PDBID: 4S0O and PDBID: 1G5M, which are correlated with biological activities and interact with the pocket of proteins with complexes through hydrophobic hydrogen bonds.

2. Experimental section

2.1. Instrumentation

Fisher–John's melting point equipment was used to determine melting points. A Mattson-5000 Fourier transform infrared (FTIR) spectrometer using the KBr disk technique was used to record the infrared spectra. Mass spectra were recorded using a Shimadzu GCMS-QP2010 Ultra (Shimadzu, Japan) equipped with an electron ionization (EI) source operated at 70 eV. Mass spectra were obtained in full scan range (m/z = 50–1000) under electron-ionization (EI) mode at 70 eV, with a dwell time of 0.3 s and detector voltage of 1.0 kV. The spectra shown represent total ion chromatogram (TIC) scans for complete EI fragmentation as opposed to tandem (MS/MS) spectra.

The University of Cairo's Microanalytical Unit performed the elemental analyses (C, H, and N). Atomic absorption was used to identify metal ions using a PerkinElmer (model 2380) spectrophotometer. A CD6NTacussel conductometer was used to measure the molar conductivity in a DMF solution (10^{-3} M). A PerkinElmer 550 spectrophotometer was used to record electronic absorption spectra in the 200–1000 nm range in DMF solution.[20] A Shimadzu TG-50 thermal analyzer was used to perform the thermal studies (differential thermogravimetry [DTG] and thermogravimetry analysis [TGA]) from room temperature to 1000 °C at a heating rate of 10 °C min^{-1}.

2.2. Chemicals and reagents

All the chemicals and solvents (HPLC grade) were acquired from Merck and had purities ranging from 99 to 99.9%. The nitrate salts of cobalt(II), nickel(II), copper(II), zinc(II), and silver(I) are Merck. Solvents used in this study were purified following the standard procedures. N^1,N^2-bis(4-phenylthiazole-2-yl) phthalamide (**PTP**) was synthesized and characterized by the published procedure. Arsenic trioxide (As_2O_3) was obtained from the Fisons Scientific Apparatus Ltd, UK in Egypt. Kits for biochemical analysis were purchased from Stanbio Co.

2.2.1. Animals. Sixty female Albino Wistar rats, aged between 7 and 9 weeks, and weighing between 160 and 180 grams, were acquired from the National Research Center animal house in Giza, Egypt. Only female rats were used to ensure consistent baseline hormonal status and reduce aggression-related stress, which can confound oxidative stress markers. Future studies will include both sexes to examine possible sex-specific differences in response to arsenic exposure and metal complex treatment. Before the experiment started, the animals were kept in polypropylene cages and allowed seven days to acclimate to specific environments free of pathogens. Rats were kept in a 12 hour light/dark cycle at 24 ± 1 °C and 55–65% humidity. The rats were given an unrestricted supply of water along with a typical rodent meal that included 17.48% protein, 6.85% fat, 62.99% carbs, 4.08% ash, and 2.16% minerals and vitamins. When working with animals, the National Institutes of Health's guide for the use and care of laboratory animals (NIH Publications No. 8023, modified 1978).

2.2.1.1. Animal grouping and treatment design. The selected sample size (n = 10) per group was determined based on previous arsenic-toxicity studies that demonstrated sufficient statistical power (≥0.8) to detect moderate effect sizes (Cohen's $d \approx 0.8$) in oxidative stress parameters. Rats were randomly divided into 6 groups; each ten rats as follows:

- Group 1: rats received normal saline for 8 weeks and were maintained as a negative control.
- Group 2: rats were injected with As_2O_3 4 mg per kg body weight for 4 weeks[21]
- Group 3: **Cu-Co-PTP** treated group that was treated with As_2O_3 (4 mg per kg body weight) for 4 weeks, then treated orally with phthalimide compound **1** at a dose of 30 mg per kg bw.[22]

• Group 4: **Cu-Ni-PTP** treated group that was treated with As_2O_3 (4 mg per kg body weight) for 4 weeks, then treated orally with phthalimide compound **2** at a dose of 30 mg per kg bw for another 4 weeks.[22]

• Group 5: **Cu-Ag-PTP** treated group that were treated with As_2O_3 (4 mg per kg body weight) for 4 weeks, then treated orally with phthalimide compound **3** at a dose of 30 mg per kg bw for another 4 weeks.[22]

• Group 6: **Cu-Zn-PTP** treated group that will be treated with As_2O_3 (4 mg per kg body weight) for 4 weeks, then treated orally with phthalimide compound **4** at a dose of 30 mg per kg bw for another 4 weeks.[22]

Although the present study focused on heterobimetallic complexes, evaluating the biological behavior of the **PTP** ligand and its homobimetallic **Cu-Cu-PTP** counterpart would provide additional mechanistic insight. Such comparisons could help determine whether the observed protective effects arise primarily from metal–metal synergism or from the ligand's intrinsic chelating and antioxidant properties. These investigations will be addressed in our future work.

2.3. Synthesis of heterobimetallic complexes

2.3.1 General procedure. Using a one-spot procedure, the novel four heterobimetallic complexes were synthesized by mixing equimolar ethanolic solutions of (2.41 g) **PTP** ligand, 10 mL (3.44 g) of copper nitrate, and 10 mL of the other metal nitrate. The previous mixture was heated to reflux at 50 °C for 2 hours with continuous stirring, then the solution evaporated to near dryness. The product was precipitated after 1 day and then filtered, washed with absolute ethanol and diethyl ether, and finally dried in a vacuum dryer over anhydrous $CaCl_2$. All the elemental analysis and analytical results (Table S1) match the suggested chemical structures quite well. According to these findings, all metal coordination compounds possess a metal : metal : ligand ratio of 1 : 1 : 1 stoichiometry.

2.4. *In vivo* analysis

2.4.1. The route of administration. As_2O_3 and different compounds were treated through oral intubation daily for 60 days was selected based on a previous study.[21] After two months, rats were fasted overnight. Anesthesia was achieved by injection of ketamine 87 mg per kg of body weight and xylazine 13 mg per kg of body weight, dissolved in normal saline, and each rat received 0.2 mL/100 g body weight.[23] Animals were sacrificed after anesthesia.

2.4.2. Blood sampling and biochemical investigations. At the end of the experimental period, blood samples were immediately collected from the retro-orbital venous plexus according to the previous method of Sorg and Buckner.[24] and left to clot in clean dry test tubes and then centrifuged at 3000 rpm for 15 minutes to obtain sera using Sigma Laborzentrifugen (Osterode am Harz, Germany). The clear supernatant sera were frozen at −20 °C. Commercial kits were purchased from Stanbio Co.

2.4.3. Lung tissue preparation. To prepare 10% (w/v) tissue homogenate, 100 mg of lung tissue was homogenized in 0.1 M phosphate buffer solution, and after centrifugation (3000 rpm for 15 min), the supernatant was collected and aliquoted in amounts of 0.5 mL to minimize intermittent freeze–thaw cycles and stored in a freezer at −80 °C (30).

2.4.4. Biochemical analyses. Glutathione reduced (GSH) and malonaldehyde (MDA) calorimetrically using spectrophotometer, and enzyme-linked immunoassay (ELIZA) for determinations of Bcl-2 and apoptotic protease-activating factor-1 (APAF-1) were purchased from Sunlong Biotech Co., Ltd, Ping Shui Street, Gong Shu District, Hangzhou, China; email: sales@sunlongbiotech.com. According the manufactures instructions, also molecular genetics investigations for mRNA expression levels of BAX, ERK, Beclin1, and LC3 genes.

2.4.5. Histopathological procedure. The fixed lung tissue specimens were trimmed, washed, and dehydrated in ascending grades of alcohol. Tissue specimens were then cleared in xylene, embedded in paraffin, sectioned at 4–6 microns thickness, stained with Hematoxylin and Eosin (H and E stain), and examined under the light microscope.[25]

2.5. Molecular analysis

2.5.1. Quantitative real-time PCR (qRT-PCR). The RNeasy mini Kit (Qiagen, Germany) (Cat. No. 74104) was used to extract RNA from rat lung tissues. To determine the concentration and purity of the total extracted RNA, the NanoDrop One microvolume UV spectrophotometer (Thermo Fisher Scientific, USA) was used. We followed the manufacturer's instructions and converted the RNA from each treatment to first-strand cDNA using the Revert Aid First Strand cDNA Synthesis Kit (Thermo Fisher Scientific, USA) (Cat. No. K1621). Quantitative RT-PCR was performed on a DTlite 4S1 real-time PCR thermocycler (DNA-Technology, Russia) using Maxima SYBR Green qPCR Master Mix (2X) (Thermo Fisher Scientific, USA) (Cat. No. K0221). Specific primer sequences for BAX, ERK, Beclin1, LC3, and β-actin are represented in Table 1, The qPCR program was: initial denaturation at 95 °C for 10 min; 40 cycles of 95 °C for 15 s, 55 °C for 30 s, 72 °C for 30 s. Relative gene expression was calculated by the $2^{-\Delta\Delta CT}$ method,[26,27] normalizing each target gene's expression to housekeeping gene β-actin and comparing all groups to the control group set to 1.

2.6. Statistical evaluation

The findings were displayed as mean ± SEM. The Tukey–Kramer multiple comparison test and one-way analysis of variances (one-way ANOVA) were used to identify statistically significant differences between the studied groups. To analyze the data, GraphPad Prism version 8 was utilized. A significant difference was considered as $p < 0.05$ for all tests.

2.7. Docking and MD simulation

PTP complexes were molecularly docked using the MOE program. The Discovery Studio Client (version 4.2) was utilized to locate it in 32,33. The Confirmation Examination module of AutoDock Vina was utilized to reduce the energy of the acquired conformations after conducting a thorough conformational analysis to an RMS gradient of 0.01, and a molecular dynamics

Table 1 Primers for qRT-PCR analysis

Gene	Forward primer (5′–3′)	Reverse primer (5′–3′)	Ref.
β-actin	CACGTGGGCCGCTCTAGGCACCAA	CTCTTTGATGTCACGCACGATTTC	28
BAX	GGGCCTTTTTGCTACAGGGT	TTCTTGGTGGATGCGTCCTG	29
ERK	GAACTCCAAGGGCTATACCAAGT	GGAGGGCAGAGACTGTAGGTAGT	30
Beclin1	CTCTGAAACTGGACACGAGC	CCTGAGTTAGCCTCTTCCTCC	31
LC3	GATAATCAGACGGCGCTTGC	ACTTCGGAGATGGGAGTGGA	31

simulation of these metal complexes was made through GROMACS[34] in water solvent with AMBER/CHARMM with metal-specific parameters at 300 K. Crystal structure of the auto-inhibited dimer of pro-apoptotic BAX (I) (PDBID: 4S0O)[35] and HUMAN BCL-2, ISOFORM 1(PDBID: 1G5M).[36] Ten distributed docking simulations were run with the default parameters. Conformations were made based on the overall data organization, the *E* conformation, and the right placement of relevant amino acids in the binding pocket of each protein.[37,38]

3. Results and discussion

3.1. Chemistry section

The four novel heterobimetallic complexes were synthesized using the one-pot procedure and the incorporation of the two different metals within the same moiety was confirmed with atomic absorption and magnetic susceptibility. All complexes exhibit higher melting points (>300 °C), and they are soluble in both DMSO and DMF solvents. The structure of the synthesized complexes, as well as the chelation nature of the neutral tetradentate **PTP** ligand, were confirmed using elemental analysis, IR, mass, H NMR, UV-visible, magnetic, and molar conductance measurements. TGA investigations were also implemented to supply more information about the geometry around the coordinated metal. Scheme 1 represents the synthesis of **PTP** ligand and its complexes.

3.2. Characterization of hetero-binuclear coordination compounds

Elemental analysis, atomic absorption, IR, UV-visible, and molar conductance measurements were used to conclude the structure of all complexes, as well as to approve the chelation nature of the tetradentate O_2N_2 donor of **PTP**.

3.2.1. FT-IR analysis. Fig. S1 and Table S2 display the IR spectra of all compounds. It was found that all of the complexes had broadbands in the 3114–3494 cm^{-1} region, which could be assigned to ν(O–H) vibration of the water molecules, whereas $\delta(H_2O)$ was observed at (1612–1639 cm^{-1}). Coordinated water molecules to the metal ions within the complexes are responsible for the bands seen at 827–852 cm^{-1}.[39] The **PTP**'s strong ν(NH) absorption bands at 3294 cm^{-1} were present in all produced complexes without any change in band position or intensity, suggesting that it did not participate in the chelation to the metal ions during complexation. The amide group's carbonyl absorption frequencies, which were detected in all of the metal complexes within (1645–1629 cm^{-1}), were lower than those of free **PTP** (1658 cm^{-1}), suggesting that the carbonyl oxygens participate in the chelation to metal ions.[40] The thiazole ring's azomethine (C=N), which was detected in all binuclear complexes between 1597 and 1560 cm^{-1}, was shifted to lower values than the free **PTP** (1613 cm^{-1}),[41] indicating that the chelation took place through the thiazole ring's N-atom. The stretching frequencies of the ν(M–O) and ν(M–N) bands appeared as weak bands in the two regions of (567–565 cm^{-1}) and (476–451 cm^{-1}), respectively,[42] indicating that **PTP** is chelated with the metal ions by the N- of the thiazole ring and the carbonyl O- of the amide group. For all complexes, the nitrate ions are unidentately attached to the metal ions with C_{2v} symmetry that has three non-degenerated vibrational modes (ν_s, ν_s' and ν_{as}), which emerged at (1406–1401 cm^{-1}), (1398–1381 cm^{-1}), and (824–816 cm^{-1}), respectively. When compared to the free nitrate group, the unidentate nitrate group's $\nu_s(NO_3^-)$ was significantly moved to lower frequencies (1700–1800 cm^{-1}).[43] This shift was ascribed to the relocation of an electron flux from the nitrate group to the metal ion, and this factor could be used to measure the covalent bond strength. In all complexes the nitrate groups also act as free ionic groups whereas the vibrations were noticed at (1759–1763 cm^{-1}) and (1361–1354 cm^{-1}) respectively.

3.2.2. Electronic spectra, magnetic, and molar conductance investigation. The electronic absorption spectrum of the **PTP** exhibited two absorption bands at 268 nm and 292 nm. The first band was attributed to π–π* transition, and the second band can be assigned to n–π* transition, while the band at 395 nm was ascribed to CT transitions to the visible area (Fig. S2). Table 2 presents the typical electronic spectral data and the evaluated magnetic moment and molar conductivity values in the DMF solvent, with which the geometry of the synthesized metal coordination compounds could be predicted with high accuracy.

In the novel four complexes, the π–π* and n–π* transitions of the ligand have shifted to higher or lower absorbance, compared to the free ligand, confirming the coordination of the free **PTP** to the metal ions to form the corresponding complexes. Magnetic susceptibility measurements are considered a crucial tool to confirm the geometrical structure of the metal complexes; in the present work, it plays an extra important role to confirm the incorporation of two different metals within the same complex. For **Cu-Co-PTP**, the μ_{eff} values for the isolated Cu(II) complexes with d^9 configuration lie in the range of 1.7–2.2 BM ($S = \frac{1}{2}$), while for isolated Co(II) with high spin d^7 ($S = 3/2$) configuration, exhibits μ_{eff} value in a range of 3.88–4.3 BM. Therefore, the existence of the two metals within the same complex **Cu-Co-PTP** will be a system with four unpaired

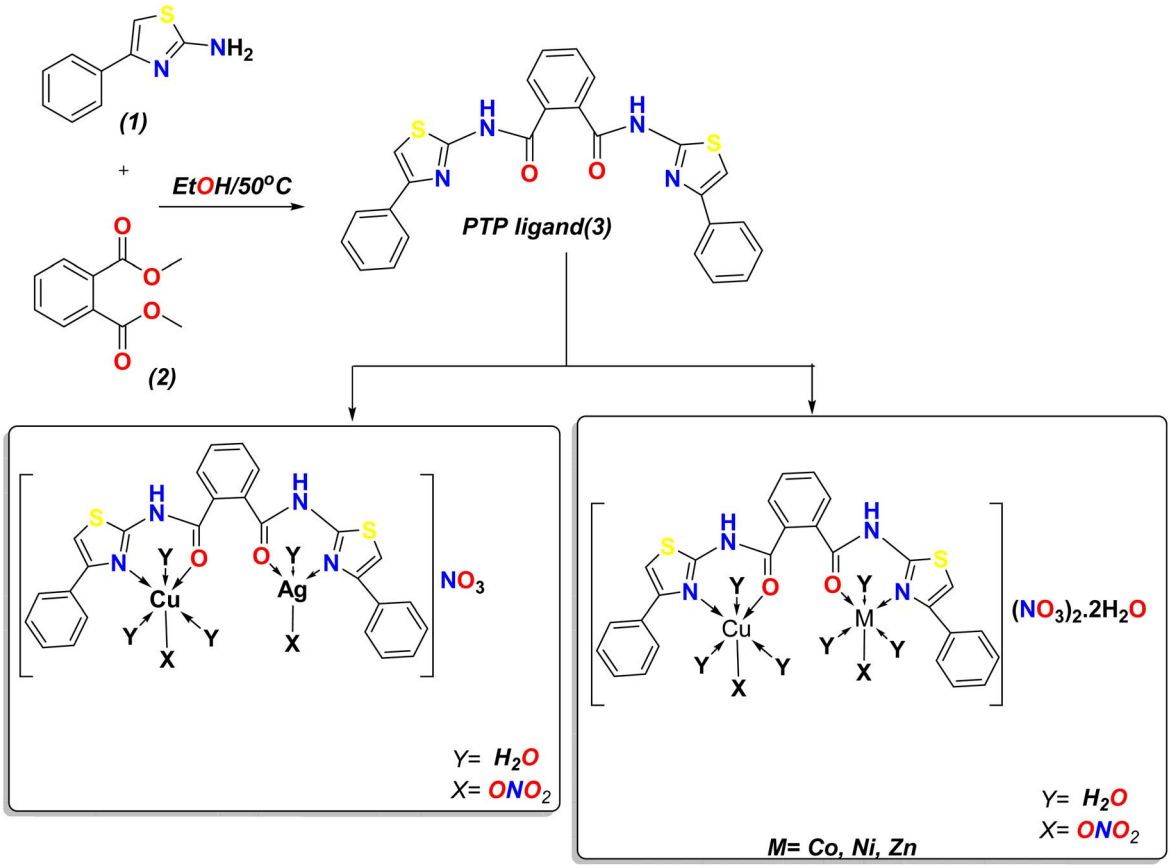

Scheme 1 Synthesis of ligand (N^1,N^2-bis(4-phenylthiazole-2-yl)phthalamide) **PTP**, and its mixed-metal complexes.

Table 2 Distinctive electronic transitions, magnetic moments, and molar conductance of all compounds

Compounds	(Electronic transition; λ_{max} (ε_{max}; cm^{-1})[a]		μ_{eff} (BM)[b]	Λ[c]
	π–π*	n–π*		
PTP	268 (0.33)	292 (0.47)	—	—
Cu-Co-PTP	263 (0.62)	322 (0.38)	4.89	131.4
Cu-Ni-PTP	265 (0.57)	327 (0.55)	3.87	127.7
Cu-Zn-PTP	216 (0.73)	363 (0.64)	1.70	100.5
Cu-Ag-PTP	288 (0.79)	325 (0.53)	1.73	81.1

[a] Electronic spectra in the visible region recorded in DMF and the values of ε_{max} are in parentheses and multiplied by 10^{-4} (mol^{-1} cm^{-1}). [b] The magnetic moment was calculated for one metal ion in the complex. [c] Molar conductance (Ω^{-1} cm^{-2} mol^{-1}) was measured in (1×10^{-3} mol^{-1} cm^{-1}) in DMF solvent.

electrons with an expected magnetic moment value of 4.90 BM. The experimental μ_{eff} values for **Cu-Co-PTP** is 4.89 BM which suggests the formation of a heterobimetallic complex with Cu(II) and Co(II) in the same structural unit. The same results obtained for the complex **Cu-Ni-PTP** confirm the existence of the Cu(II) and Ni(II) both with octahedral geometries in the same complex where in case of octahedral Ni(II) with d^8 configuration the magnetic moment value of 2.83 BM is expected, therefore the resulting complex will be a system with three unpaired electrons with expected μ_{eff} of 3.88 BM. Consequently, the experimental measured μ_{eff} with 3.87 BM confirms the suggested complex structure. With respect to the two complexes **Cu-Zn-PTP** and **Cu-Ag-PTP**, the Zn(II) or Ag(I) with d^{10} configuration and tetrahedral geometry, the measured μ_{eff} of 1.7 BM and 1.72 BM respectively is an expected result for the unpaired electron related to Cu(II) core in both heterobimetallic complexes, which confirms again the suggested structures. The suggested structures for all heterobimetallic complexes were further confirmed by the molar conductance values which was found to be 131.4 and 127.7 ohm^{-1} cm^{-2} mol^{-1}, for the **Cu-Co-PTP** and **Cu-Ni-PTP** complexes, respectively, which means that these complexes are in the 1 : 2 electrolytes while the molar conductivity for the remaining complexes **Cu-Zn-PTP** and **Cu-Ag-PTP** are 81.1 and 100.5 ohm^{-1} cm^{-2} mol^{-1}, which means that these complexes are in the 1 : 1 electrolyte.[44]

3.2.3. Mass spectra analysis. An additional method for confirming the suggested structures was mass spectrometry. The SI files (Fig. S3–S7) represent the mass spectra for the ligand **PTP** and all complexes, while Fig. S8–S10 show the fragmentation patterns of the ligand, **Cu-Co-PTP**, and **Cu-Zn-PTP** complexes, respectively. The mass spectra for the ligand and its complexes correspond to the fragmentation spectra, where the fragments were assigned depending on the suggested fragmentation pathways. The suggested structure of the **PTP** ligand

was validated through recorded mass spectra (Fig. S3), which showed a peak at 481.91 *m*/*z* representing the radical cation $[M]^{+\cdot}$. The proposed structure aligns excellently with the series of mass-to-charge ratios (*m*/*z*) represented by the peaks: 52.99 (100% base peak), 66.07 (31%), 77.95 (16%), 135.18 (8%), 167.27 (28%), 246.9 (31%), 334.98 (6%), and 405.12 (9%). Scheme S1 illustrates the fragmentation pattern of the **PTP** ligand. For the **Cu-Co-PTP** complex, a parent peak was noticed at 997.95 *m*/*z* due to the molecular ion M, which is consistent with the complex's M.wt (997.20 g $mole^{-1}$). Additionally, the mass spectrum showed the appearance of a parent peak at *m*/*z* of 483.11 (27%) that corresponds to the M.wt of the **PTP** ligand and other parent peaks at *m*/*z* = 63.07, 65.16, and 60.19 which reflect the combined isotopic distribution of the two metals Cu and Co, respectively. This finding confirms again their coexistence within the same ligand framework. The base peak appeared at 364.21 *m*/*z*, while a series of peaks emerged at 76.01 (81.34%), 102.97 (66.25%), 252.60 (54.22%), 280.59 (78.12%), 364.21 (100.00%), 465.63 (57.23%), 601.54 (58.25%), 835.21 (45.77%) *m*/*z*, and 997.95 (34.22%). Similar observations were found for the remaining heterobimetallic complexes, and all mass spectral data were displayed in Table S3.

The fragmentation spectra seen in Fig. S3–S7 are full-scan electron-ionization (EI) mass spectra recorded in the mass/charge (*m*/*z*) range of 50–1000, using a Shimadzu GC-MS-QP2010 Ultra instrument at 70 eV. The full MS range was turned on for acquisition, which gives complex but reproducible fragmentation profiles that reflect both the thiazole–phthalimide ligand and the coordinated nitrate and water moieties. The apparent congestion of peaks with well-resolved *m*/*z* values reflects the fragmentation of multiple subunits instead of distinct MS/MS isolation and identification of a subunit fragment. Major fragments represent successive losses of H_2O, NO_3^-, C_3HNS, phenyl groups, and other species associated with the ligand fragments, as expected from the proposed structure and data in Table S3. For clarity, this methodological comment is now in the Experimental section, reinforcing that these fragmentation spectra represent complete EI full-scan fragmentation and are not tandem product-ion spectra.

3.2.4. H NMR analysis for PTP. The theoretical and experimental ^{1}H NMR spectra of **PTP** show an excellent agreement, as shown in Fig. S11. Both the CH of the thiazole ring and the NH of the amide group were assigned to the experimental bands that formed in the range of 7.82–6.98, which matched the theoretical multiplet bands that developed in the 7.90–7.31 ppm range. The interference of the various aromatic protons prevented the signals in this range from being resolved. **PTP** binds to the metal ions *via* the N- of the thiazole ring and the O- of the carbonyl of the amide group, as demonstrated by Fig. S11, which also shows that the protonated and deprotonated **PTP** ligand spectra do not differ, indicating the absence of a replaceable hydrogen atom.

3.3. TGA study

In the present work, thermal analysis was carried out to get significant information about the thermal stability of the prepared complexes and to inspect the nature of solvent molecules (if existing) inside the inner coordination sphere of the metal or outside it.[45–47] Fig. 1 represents the TGA for **Cu-Co-PTP** complex, while Fig. S12 depicts TGA for the remaining complexes. The thermogram of the **Cu-Co-PTP** complex involves four consecutive stages (Table S4). The first started at 78 °C to 210 °C for the removal of 2 uncoordinated H_2O and 6 coordinated H_2O molecules, followed by a weight loss of 11.01% (calc., 10.85%). At the temperature range of (215–289 °C), the second stage revealed the removal of $2N_2O_5$ and O_2 molecules, accompanied by a loss of 25.67% (calc., 24.89%). In addition, the third stage was noticed at (290–367 °C) due to the loss of two phenyl groups of the thiazole moiety, followed by an experimental mass disappearance of 17.02% (calc., 15.48%). Finally, the remaining organic ligand was eliminated at the temperature range of (370–475 °C) with experimental weight loss of 30.71% (calc. 32.95%). The final residual weight matched copper oxide and cobalt oxide (calc. 15.49%). Table S4 showed the detailed thermoanalytical results for all degradation stages for the remaining complexes.

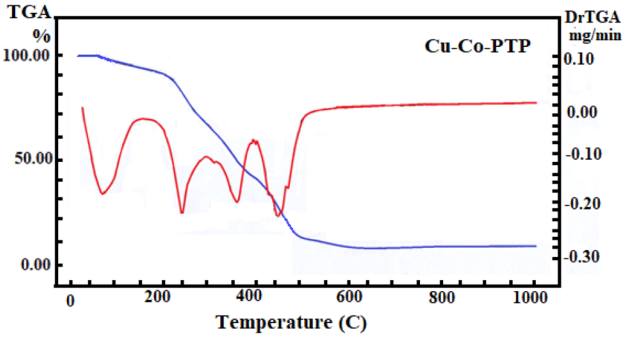

Fig. 1 TGA/DTG curves for Cu-Co-PTP complex.

4. XRD investigation

XRD is one of the most crucial instruments used to get structural microcrystalline information about the compounds under investigation. The newly produced heterobimetallic complexes are solvent soluble in DMSO and DMF; however, no appropriate crystals were found for single crystal examination. Powder X-ray diffraction is a method for determining the degree of crystallinity of metal complexes. All-metal complexes in the 4–70 (θ) range were analyzed at 1.54 Å. Since solid frameworks are rarely configured during the precipitation process, all X-ray diffraction curves (Fig. 2) demonstrate the somewhat amorphous nature of all heterobimetallic complexes. Bragg's law can be applied to compute the interplanar distance *d* (the volume average of the crystal dimension normal to the diffracting plane) from 2θ variable:[14,42] $2d \sin\theta = n\lambda$ where λ is the symbol of incident wave wavelength and *n* is a positive integer.

Moreover, the crystallinity index (CI) can be calculated using the equation[2] $\mathrm{CI} = \frac{A_c}{A_c + A_a}$, where A_c is the area under crystalline peaks and A_a is the area under amorphous hollows. The CI values for the **Cu-Co-PTP**, **Cu-Ni-PTP**, **Cu-Zn-PTP**, and **Cu-Ag-**

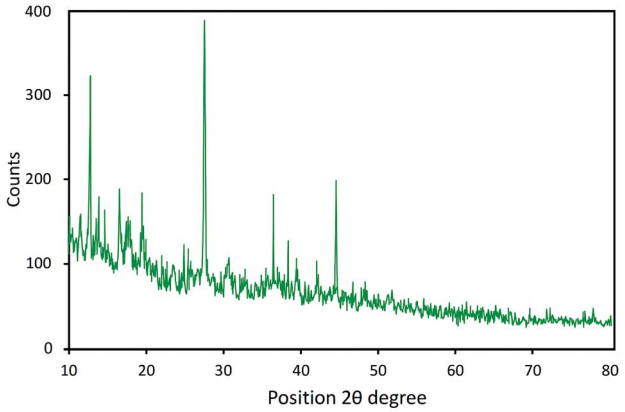

Fig. 2 XRD pattern for **Cu-Co-PTP** complex.

Table 3 Powder XRD data for **Cu-Co-PTP** complex

			d-spacing [Å]					
Peak	θ	Sin θ	Obs.	Calc.	FWHM	h	k	l
1	8.1103	0.1411	5.4191	5.4571	0.1590	1	0	0
2	9.0512	0.1573	4.8907	4.8951	1.1936	1	0	0
3	10.6104	0.1841	4.1829	4.1825	0.2787	1	1	0
4	15.2274	0.2627	2.9412	2.9311	0.4952	1	1	1
5	17.0011	0.2924	2.6367	2.6334	0.2923	2	0	0
6	19.7654	0.3382	2.2770	2.2768	0.9446	2	1	0
7	23.8022	0.4036	1.9168	1.9078	0.3149	2	1	1
8	29.3887	0.4907	1.5701	1.5691	0.2362	2	2	0
9	32.4875	0.5371	1.4341	1.4336	0.2558	2	2	1
						3	0	0
10	38.9945	0.6292	1.2237	1.2238	0.2362	3	1	1

PTP complexes are 39.8, 47.4, 61.2 and 59.5; respectively. Bragg's equation, $n\lambda = 2d \sin\theta$, was used to calculate the inter-planar spacing (d), which looked to be in good accord with the measured values. Table 3 shows the observed and computed inter-planar d spacing, values of 2θ, and Miller indices (hkl) for the most intense peaks for **Cu-Co-PTP**. The values of $h^2 + k^2 + l^2$ were determined to be 1, 2, 3, 4, 5, 6, 8, 9, 10, 11 and 13. The lack of the forbidden numbers (7 and 15) demonstrates cubic symmetry.

5. SEM investigation

The **Cu-Ni-PTP** and **Cu-Ag-PTP** complexes were chosen as an example to study its surface morphology since they revealed the highest value of the crystallinity index. The SEM images of complexes at a magnification of 2.500 are shown in Fig. 3. For **Cu-Ag-PTP**, a rock-like appearance was shown and a large territorial patch. The micrographs of the **Cu-Ni-PTP** complex, on the other hand, showed well-defined crystals with a twisted fiber and grass-like shape that were free from any shadow of the metal ion on their external surface. According to the SEM analysis, crystals were found to develop in all of the produced metal complexes, from a single molecule to multiple molecules in an aggregate distribution with particle sizes ranging from a few nanometers to several hundred.

6. Biological activity evaluation

6.1. *In vivo* analysis

The levels of MDA and GSH activity in lung tissue homogenates across different experimental groups are presented in Fig. 4A and B. As_2O_3-intoxicated rats showed a significant increase in tissue MDA levels ($p < 0.001$) and a significant decrease in GSH enzyme activity ($p < 0.001$) level compared to the control group. However, co-administration of the newly synthesized TPHC complexes for 30 days resulted in a marked reduction in MDA levels ($p < 0.001$) relative to the As_2O_3-treated group. Furthermore, treatment with TPHC complexes significantly restored GSH enzyme activity ($p < 0.05$) level compared to As_2O_3-exposed animals. These data confirm that TPHC complexes effectively mitigate As_2O_3-induced oxidative stress in lung tissue by reducing lipid peroxidation and enhancing antioxidant capacity. Similarly, the levels of Bcl-2 and APAF-1 in lung tissue homogenates are illustrated in Fig. 4C and D. A significant elevation in Bcl-2 and APAF-1 levels was observed in the As_2O_3-treated group compared to the control group ($p < 0.001$), suggesting increased apoptotic signaling in response to As_2O_3-induced lung toxicity. Notably, co-treatment with TPHC complexes significantly attenuated these elevations ($p < 0.01$), indicating a potential anti-apoptotic effect of the compounds. These results support the anti-apoptotic potential of TPHC

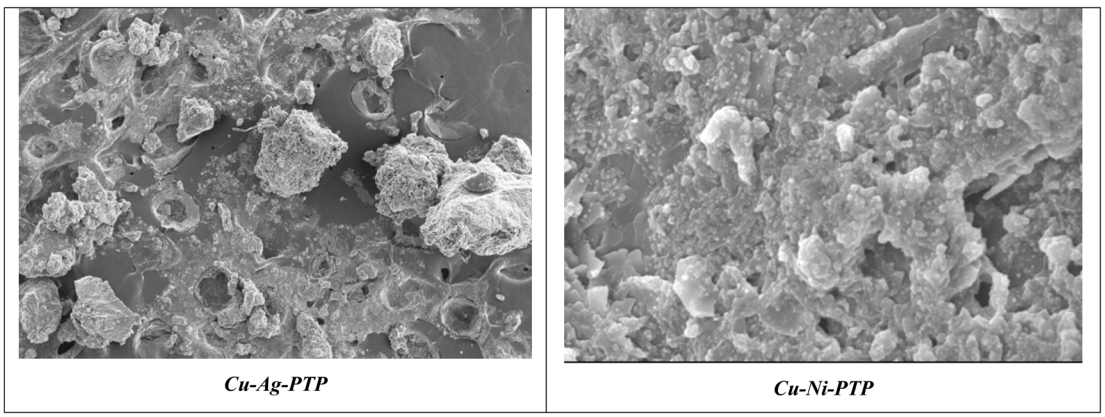

Fig. 3 SEM micrographs of **Cu-Ni-PTP** and **Cu-Ag-PTP** complexes.

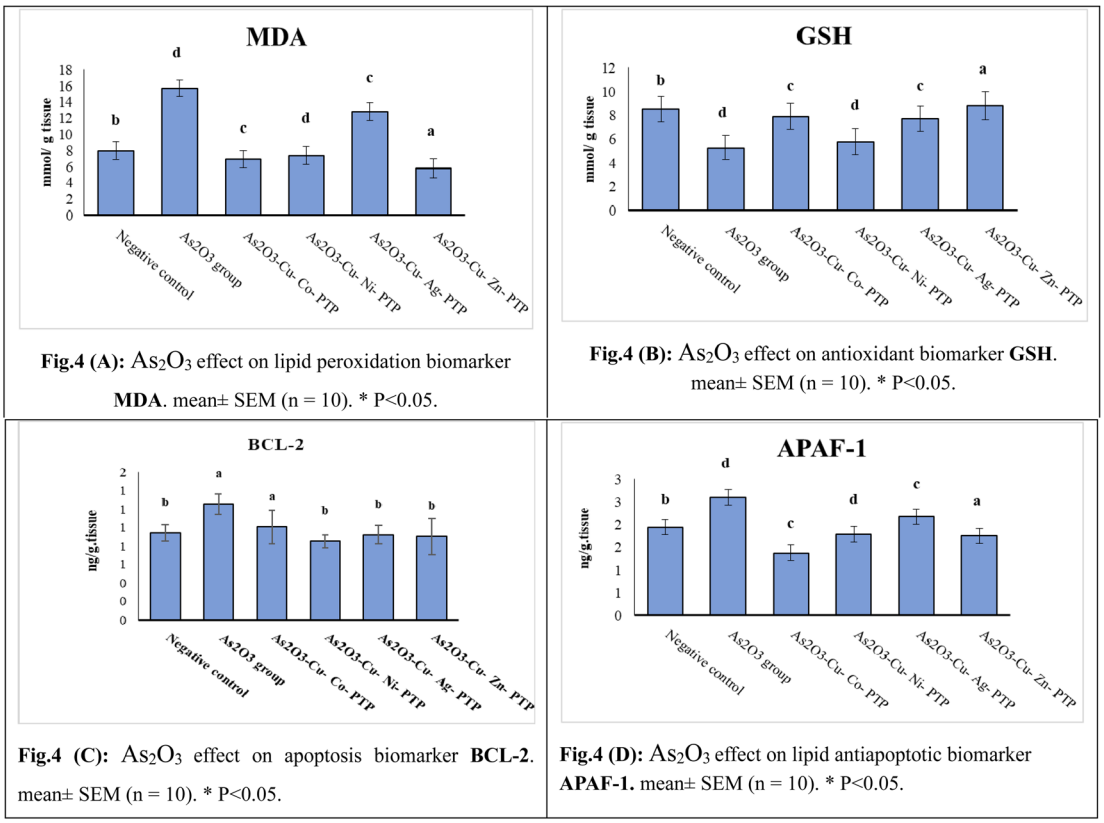

Fig.4 (A): As_2O_3 effect on lipid peroxidation biomarker **MDA**. mean± SEM (n = 10). * P<0.05.

Fig.4 (B): As_2O_3 effect on antioxidant biomarker **GSH**. mean± SEM (n = 10). * P<0.05.

Fig.4 (C): As_2O_3 effect on apoptosis biomarker **BCL-2**. mean± SEM (n = 10). * P<0.05.

Fig.4 (D): As_2O_3 effect on lipid antiapoptotic biomarker **APAF-1.** mean± SEM (n = 10). * P<0.05.

Fig. 4 (A–D) Tissue biochemical parameters of Wistar rats exposed to As_2O_3 (4 mg per kg body weight). Data are presented as the means ± SE $n = 10$. Data were analyzed by ANOVA one-way. $P \leq 0.05$, value with the same letter has no significance, but value with the different letter has significant at 0.05.

complexes in alleviating As_2O_3-induced lung injury through modulation of key regulators in the mitochondrial apoptotic pathway.

6.2. Histopathological examination

Histological examination of hematoxylin and eosin (H&E)-stained lung tissue sections revealed significant structural alterations among the experimental groups (Fig. 5A–L).

In the control group (G1), the lung architecture appeared normal, with bronchioles lined by a single layer of ciliated epithelium and alveoli displaying intact, sac-like structures lined with alveolar epithelium (Fig. 5A and B).

In contrast, the As_2O_3-intoxicated group (G2) showed marked histopathological damage, including hemorrhagic inflammation of the interstitial lung tissue, extravasation of red blood cells (RBCs), deposition of hemosiderin pigment, and the presence of giant alveoli (Fig. 5C and D). The G3 group (As_2O_3 + **Cu-Co-PTP**) exhibited moderate improvement in lung architecture. Although some alterations persisted, such as mucous exudate with cellular debris in the bronchiolar lumen, congested peribronchial blood vessels, and inflammatory cell infiltration, the overall lung structure was less severely affected (Fig. 5E and F). The G4 group (As_2O_3 + **Cu-Ni-PTP**) showed mild histopathological improvement. However, signs of injury remained, including cell debris within bronchioles, reduced elasticity of the alveolar walls resulting in giant alveoli, and interstitial inflammation accompanied by edema (Fig. 5G and H). The G5 group (As_2O_3 + **Cu-Ag-PTP)** demonstrated histological features of bronchial epithelial hyperplasia, mucous exudate mixed with cellular debris in the bronchial lumen, thickened peribronchial blood vessel walls, and widespread interstitial inflammatory infiltration, along with giant alveoli (Fig. 5I and J). Notably, the G6 group (As_2O_3 + **Cu-Zn-PTP**) displayed the most marked histological improvement among the treated groups. Bronchiolar epithelium appeared largely restored, alveolar structures were preserved, and only focal areas of inflammatory cell aggregation were noted (Fig. 5K and L). These findings suggest that the TPHC complexes, particularly **Cu-Zn-PTP**, confer protective effects against As_2O_3 -induced pulmonary injury, likely by preserving lung tissue architecture and reducing inflammation.

To our knowledge, this is the first *in vivo* study evaluating the impact of thiazole–phthalimide-based heterobimetallic complexes on oxidative stress markers in rat lung tissue. While extensive literature exists on their anticancer and antioxidant properties in systemic or *in vitro* models, none directly assess MDA, GSH levels in pulmonary tissue. Thus, our findings fill a critical gap in the field, demonstrating the compounds' ability to reduce lipid peroxidation (MDA) and enhance antioxidant GSH enzyme activities in lung homogenates. These effects align

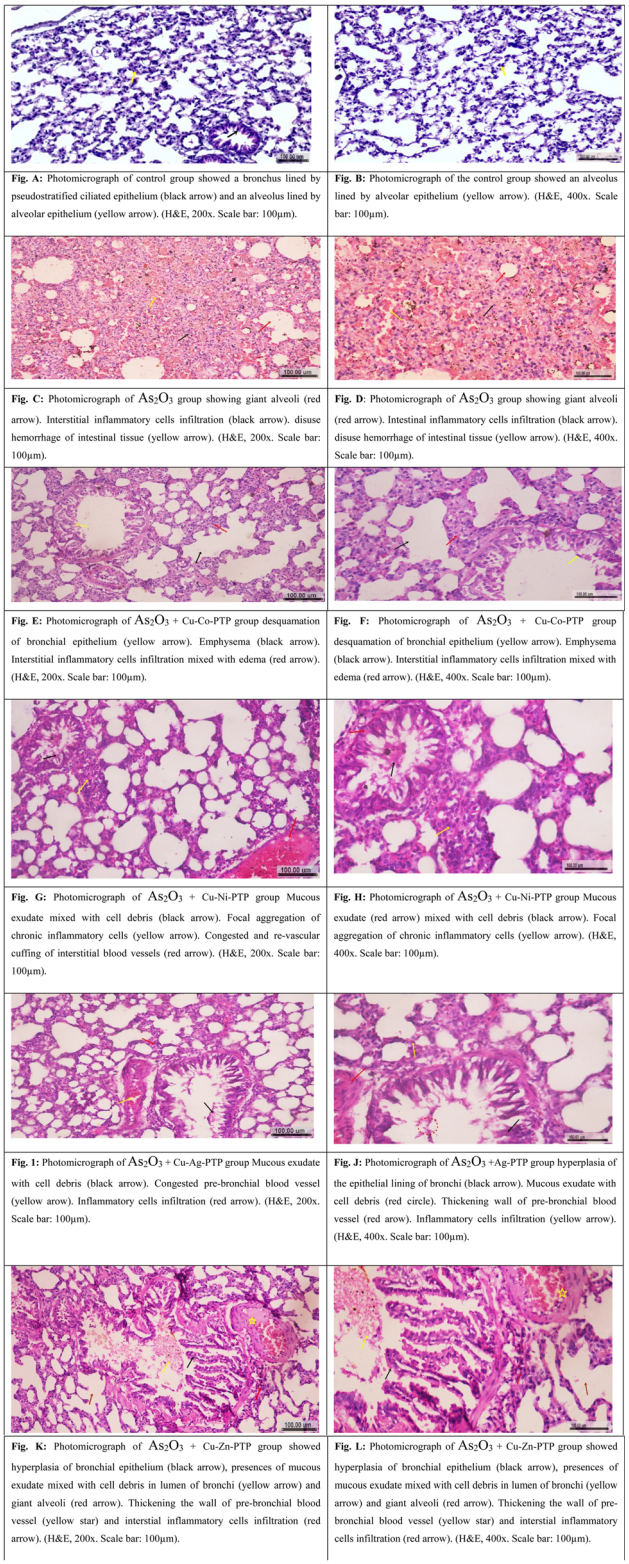

Fig. A: Photomicrograph of control group showed a bronchus lined by pseudostratified ciliated epithelium (black arrow) and an alveolus lined by alveolar epithelium (yellow arrow). (H&E, 200x. Scale bar: 100μm).

Fig. B: Photomicrograph of the control group showed an alveolus lined by alveolar epithelium (yellow arrow). (H&E, 400x. Scale bar: 100μm).

Fig. C: Photomicrograph of As_2O_3 group showing giant alveoli (red arrow). Interstitial inflammatory cells infiltration (black arrow). disuse hemorrhage of intestinal tissue (yellow arrow). (H&E, 200x. Scale bar: 100μm).

Fig. D: Photomicrograph of As_2O_3 group showing giant alveoli (red arrow). Intestinal inflammatory cells infiltration (black arrow). disuse hemorrhage of intestinal tissue (yellow arrow). (H&E, 400x. Scale bar: 100μm).

Fig. E: Photomicrograph of As_2O_3 + Cu-Co-PTP group desquamation of bronchial epithelium (yellow arrow). Emphysema (black arrow). Interstitial inflammatory cells infiltration mixed with edema (red arrow). (H&E, 200x. Scale bar: 100μm).

Fig. F: Photomicrograph of As_2O_3 + Cu-Co-PTP group desquamation of bronchial epithelium (yellow arrow). Emphysema (black arrow). Interstitial inflammatory cells infiltration mixed with edema (red arrow). (H&E, 400x. Scale bar: 100μm).

Fig. G: Photomicrograph of As_2O_3 + Cu-Ni-PTP group Mucous exudate mixed with cell debris (black arrow). Focal aggregation of chronic inflammatory cells (yellow arrow). Congested and re-vascular cuffing of interstitial blood vessels (red arrow). (H&E, 200x. Scale bar: 100μm).

Fig. H: Photomicrograph of As_2O_3 + Cu-Ni-PTP group Mucous exudate (red arrow) mixed with cell debris (black arrow). Focal aggregation of chronic inflammatory cells (yellow arrow). (H&E, 400x. Scale bar: 100μm).

Fig. I: Photomicrograph of As_2O_3 + Cu-Ag-PTP group Mucous exudate with cell debris (black arrow). Congested pre-bronchial blood vessel (yellow arow). Inflammatory cells infiltration (red arrow). (H&E, 200x. Scale bar: 100μm).

Fig. J: Photomicrograph of As_2O_3 +Ag-PTP group hyperplasia of the epithelial lining of bronchi (black arrow). Mucous exudate with cell debris (red circle). Thickening wall of pre-bronchial blood vessel (red arow). Inflammatory cells infiltration (yellow arrow). (H&E, 400x. Scale bar: 100μm).

Fig. K: Photomicrograph of As_2O_3 + Cu-Zn-PTP group showed hyperplasia of bronchial epithelium (black arrow), presences of mucous exudate mixed with cell debris in lumen of bronchi (yellow arrow) and giant alveoli (red arrow). Thickening the wall of pre-bronchial blood vessel (yellow star) and interstial inflammatory cells infiltration (red arrow). (H&E, 200x. Scale bar: 100μm).

Fig. L: Photomicrograph of As_2O_3 + Cu-Zn-PTP group showed hyperplasia of bronchial epithelium (black arrow), presences of mucous exudate mixed with cell debris in lumen of bronchi (yellow arrow) and giant alveoli (red arrow). Thickening the wall of pre-bronchial blood vessel (yellow star) and interstial inflammatory cells infiltration (red arrow). (H&E, 400x. Scale bar: 100μm).

Fig. 5 (A–L) Histological examination of lung tissue.

with known antioxidant trends observed in other organ systems, but extend their relevance specifically to pulmonary oxidative injury. In this regard, free radicals lead to lipid peroxidation (LPO) and produce active aldehydes such as malondialdehyde. These byproducts are used as efficient diagnostic biomarkers to assess the severity of oxidative damage.[48]

In this study, As_2O_3 exposure markedly increased lung tissue malondialdehyde (MDA) levels and decreased glutathione (GSH) activity—clear indicators of induced oxidative stress. These findings corroborate Muthumani *et al.*,[49] who demonstrated that As_2O_3 promotes reactive oxygen species (ROS) generation: its cationic form transfers an unpaired electron to molecular O_2, producing superoxide radicals. These highly reactive species attack unsaturated fatty acids, leading to lipid peroxidation and the disruption of lung cell membranes *via* fatty acid hydroperoxides.[49] Additionally, As_2O_3 harmful effects may extend to oxidative DNA damage, beyond nitrative mechanisms. Conversely, treatment with the tested compounds prevented the As_2O_3-induced increase in MDA and the decline in GSH activity, highlighting their antioxidant and lipid-peroxidation–inhibiting properties. These protective effects are likely due to hydroxyl groups in their structure, as well as the well-established ROS scavenging potential of thiazole and phthalimide moieties. El-Aarag *et al.*[22] similarly demonstrated that a phthalimide analog counteracted CCl_4-induced lipid peroxidation in liver tissues, reducing MDA while enhancing antioxidant enzyme levels highlighting its oxidative stress attenuating capacity.

In the present study, treatment with the Cu–Ni complex resulted in a modest improvement in antioxidant enzyme activities compared with the arsenic-intoxicated group; however, its efficacy was significantly lower than that observed with the Cu–Co and Cu–Zn complexes. This finding suggests that the biological behavior of each complex is influenced by differences in metal–ligand interaction strength, redox potential, and stability under physiological conditions. Copper-containing complexes are generally known for their strong redox activity, which allows facile cycling between Cu(II) and Cu(I) states, thereby enhancing reactive oxygen species (ROS) scavenging and promoting antioxidant defense mechanisms.[50] In contrast, nickel-containing complexes tend to exhibit lower redox flexibility and weaker electron-transfer capacity, which may account for their diminished antioxidant performance.[51] Collectively, these findings underscore the importance of metal identity and coordination chemistry in determining the antioxidant and cytoprotective potential of thiazole–phthalimide-based heterobimetallic complexes.

Our results align with recent evidence supporting the role of structurally diverse antioxidants in mitigating arsenic-induced toxicity. For example, quercetin, a hydroxyl-rich flavonoid, significantly reversed arsenic-induced oxidative alterations by restoring superoxide dismutase (SOD) and GSH-peroxidase activities while reducing MDA and protein carbonyl content.[52] Similarly, *N*-acetylcysteine (NAC), a GSH precursor, was shown to protect against arsenic toxicity in multiple organs, including lung, by replenishing intracellular GSH, scavenging ROS, and attenuating inflammatory responses.[53] Collectively, these findings suggest that the protective effects of the tested compounds in the current study are comparable to those of other known antioxidants. The ability of these agents to scavenge ROS, restore antioxidant defense systems, and reduce lipid

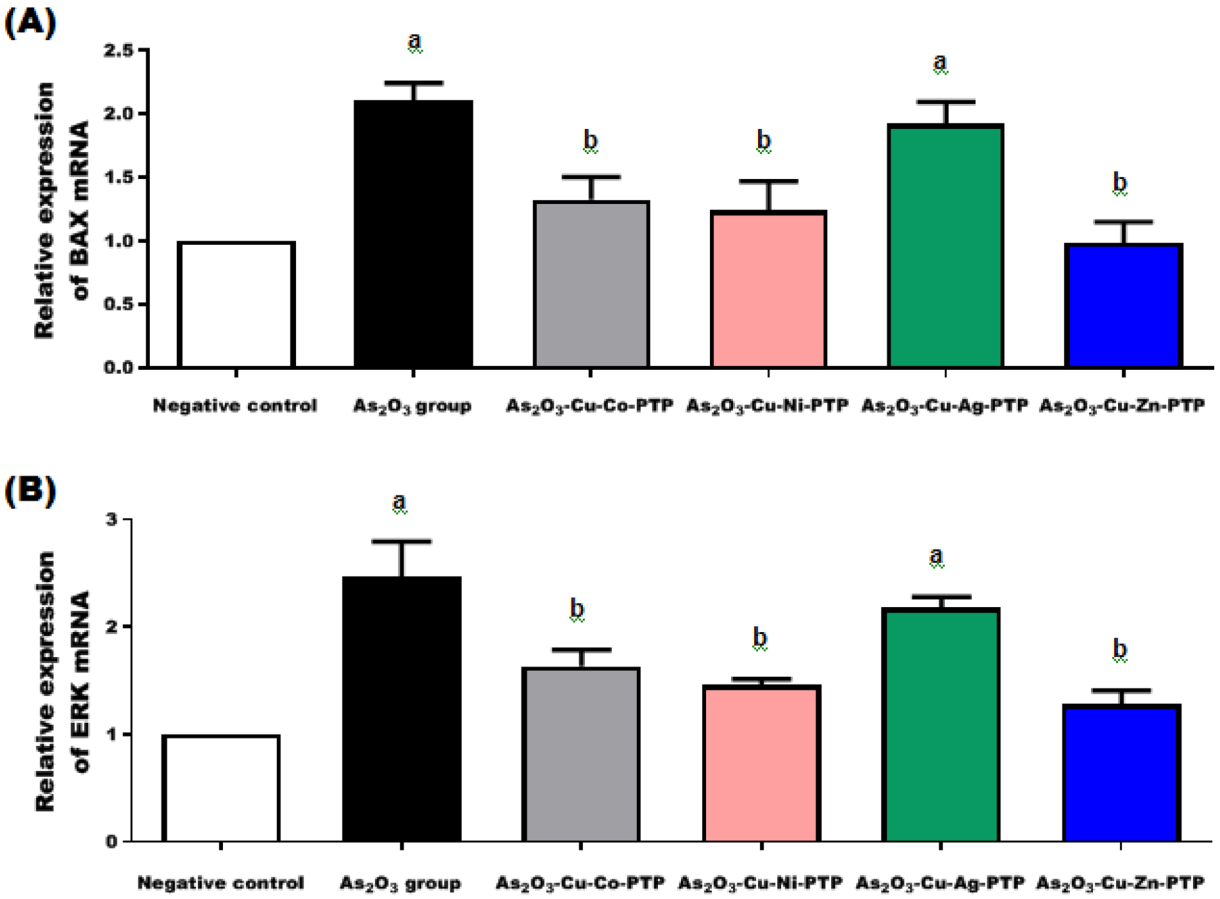

Fig. 6 (A and B) Investigation of the apoptosis-related genes BAX and ERK in the studied groups using real-time polymerase chain reaction. One-way ANOVA was used to analyze the data, and then the Tukey–Kramer multiple comparison test was used. Every value ($n = 6$) was shown as mean ± SEM. [a] $p < 0.05$ in comparison to the control group; [b] $p < 0.05$ in comparison to the group that was treated with As_2O_3.

peroxidation underscores their therapeutic potential in mitigating arsenic-induced pulmonary toxicity. Importantly, the structural features of thiazole and phthalimide moieties may provide a valuable pharmacophore for the development of novel antioxidant therapeutics. As_2O_3 induces apoptosis in lung tissue mainly *via* the intrinsic mitochondrial pathway through Cytochrome c release, Apaf-1 activation, and caspase cascade-mediated cell death. It upregulates pro-apoptotic proteins (Bax, Apaf-1), promotes PARP cleavage, and activates both intrinsic and extrinsic pathways, possibly involving MAPK upregulation and Akt suppression.[55,56]

In the present study, arsenic-intoxication caused severe histopathological changes in rat lungs, including interstitial hemorrhage, RBC extravasation, hemosiderin-laden macrophages, and giant alveoli formation. These alterations are attributed to oxidative stress, lipid peroxidation, and free radical accumulation, which impair membrane integrity and promote inflammation.[54] Consistent with earlier reports, As_2O_3 exposure has been shown to induce alveolar wall rupture, edema, interstitial thickening, hemorrhage, and inflammatory infiltration, leading to disruption of alveolar-capillary integrity and vascular permeability.[29,55,56] Arsenic exposure in the present study caused severe lung injury, including alveolar wall damage, edema, and inflammatory infiltration, consistent with earlier reports that arsenic induces pulmonary toxicity through ROS generation and oxidative stress.[57] The protective effects of thiazole–phthalimide heterobimetallic complexes varied depending on the coordinated metal. **Cu-Co-PTP** and **Cu-Ni-PTP** showed only mild to moderate protection, reducing inflammatory aggregates but failing to fully restore alveolar architecture. This is in line with evidence that cobalt- and nickel-based compounds provide limited antioxidant defense.[58] Conversely, **Cu-Ag-PTP** was associated with epithelial hyperplasia, mucous exudates, and persistent inflammation, reflecting previous findings that silver complexes can provoke lung inflammation.[59] The most significant histological recovery was observed with **Cu-Zn-PTP**, which preserved bronchiolar epithelium and restored alveolar structure with minimal inflammation. This superior effect is attributed to the well-documented synergistic antioxidant and anti-inflammatory activities of zinc and copper.[60] Collectively, these findings highlight the critical role of metal ion selection in the design of organometallic therapeutics. Among the tested complexes, **Cu-Zn-PTP** appears to be the most promising candidate for mitigating arsenic-induced pulmonary injury.

Table 4 Relative mRNA expression levels of BAX, ERK, Beclin1, and LC3, presented as fold-change ($2^{-\Delta\Delta CT}$ values)

Groups	Genes			
	$2^{-\Delta\Delta CT}$ values of BAX gene	$2^{-\Delta\Delta CT}$ values of ERK gene	$2^{-\Delta\Delta CT}$ values of Beclin1 gene	$2^{-\Delta\Delta CT}$ values of LC3 gene
Negative control	1	1	1	1
As_2O_3 group	2.1	2.5	7.4	3.9
As_2O_3-**Cu-Co-PTP**	1.3	1.6	6.3	3.1
As_2O_3-**Cu-Ni-PTP**	1.2	1.5	2.8	2.2
As_2O_3-**Cu-Ag-PTP**	1.9	2.2	6.01	3.4
As_2O_3-**Cu-Zn-PTP**	0.9	1.3	2.5	2.1

6.3. Molecular outcomes

Arsenic triggers apoptosis by increasing BAX and Caspase-3 while reducing BCL2, with arsenic trioxide enhancing oxidative stress, inflammation, and uterine cell death.[61–63] Additionally, it suppresses mitophagy, reflected by a decreased BCL2/BAX ratio.[64] At the signaling level, low arsenite doses activate ERK to promote proliferation, while higher doses trigger apoptosis *via* JNK signaling.[65] Arsenic-driven cellular transformation involves ERK and P38 pathway activation alongside JNK inhibition, resulting in decreased pro-apoptotic (BAX) and increased anti-apoptotic (BCL2, BCL-XL) proteins. Furthermore, arsenic-induced ROS enhances angiogenesis by activating AKT and ERK1/2 pathways, upregulating VEGF and HIF-1 expression.[65] Our results corroborate the aforementioned facts since we discovered that the arsenic group had significantly ($p < 0.05$) greater levels of mRNA expression for the apoptotic genes BAX and ERK by around 110% and 140% of the normal control group, respectively (Table 4, Fig. 6A and B). According to Medda *et al.*,[65] As_2O_3 can downregulate BCL2, BCL-XL, and MCL-1 and upregulate pro-apoptotic proteins including BAX, BAD, BMF, and BIM. Additionally, arsenic can activate src kinase, which aids in EGFR and ERK 1/2 activation. Zhong *et al.*[66] also noted the effects of Sb and/or ATO on liver tissue apoptosis. In liver tissues, the ATO + Sb group's mRNA levels of Caspase-3, Caspase-9, BAX, P53, and Cytc were considerably ($p < 0.05$) higher than those of the control group. Conversely, we observed that the expression levels of BAX and ERK were significantly lower in the As_2O_3-**Cu-Zn-PTP**, As_2O_3-**Cu-Ni-PTP**, and As_2O_3-**Cu-Co-PTP** treated groups (by about 53% and 48% for As_2O_3-**Cu-Zn-PTP**; 41% and 42% for As_2O_3-**Cu-Ni-PTP**; 37% and 35% for As_2O_3-**Cu-Co-PTP**, respectively), especially in the As_2O_3-**Cu-Zn-PTP** treated group, compared to the arsenic group ($p < 0.05$) (Table 4, Fig. 6A and B). This result is consistent with that of Rahaman *et al.*,[67] who showed that P53, BAX, cytosolic Cytochrome *c*, Caspase 9, and cleaved/active Caspase 3 were significantly downregulated during co-exposure to curcumin (2.5 μM) and As^{3+} (10 μM). Trace levels of heavy metals are present in live animals and contribute to a variety of biological processes in addition to being present in numerous environmental areas. For example, iron (Fe) is vital for oxygen transport and nucleic acid synthesis, copper (Cu) is found in nearly all organs and is required for a number of metabolic activities, and zinc (Zn) is not only structurally significant but also has a regulatory function.[68]

Autophagy maintains cellular homeostasis, while apoptosis mediates programmed cell death; their interplay can be synergistic or antagonistic depending on conditions like cancer, ageing, and stress.[69] Beclin1, a key autophagy regulator on chromosome 17q21, functions *via* the PI3KC3 complex or interaction with BCL2.[70] It has therapeutic potential by reducing inflammation in sepsis. Under arsenic exposure, IL-6/STAT3 signaling promotes MCL1-Beclin1 binding, suppressing apoptosis.[71] Another important indicator of autophagosomes is LC3, whose conversion to LC3-II marks autophagosome formation, while P62 mediates selective degradation.[72] Arsenic trioxide induces autophagy prior to apoptosis in foam cells and macrophages, as shown by increased LC3-II/LC3-I and decreased P62, followed by activation of apoptotic markers such as cleaved Caspase-3 and Caspase-9. These findings suggest that arsenic trioxide sequentially triggers autophagy and apoptosis depending on cellular context.[73] In the present study, autophagic genes Beclin1 and LC3 were about 640% and 290% significantly greater ($p < 0.05$) in the arsenic group than in the control group (Table 4, Fig. 7A and B). These results confirm those of Saha *et al.*,[73] who showed that autophagy was initiated by downstream activation of mitophagic and autophagic molecules (Beclin1, PINK1, Parkin 1, LCIIIB) in response to arsenic poisoning in the brain caused by PLCβ1 activating ERK1/2. Additionally, LC3 and P62 were shown to co-localize in some cells, and arsenic increased their expression.[74] Moreover, arsenic trioxide (2.5 μM) elevated the LC3II/LC3I ratio, P62 degradation, and the levels of Atg5, Atg7, and Beclin1 mRNA in macrophages in comparison to control cells. On the other hand, our observations displayed that the As_2O_3-**Cu-Zn-PTP**, As_2O_3-**Cu-Ni-PTP**, As_2O_3-**Cu-Co-PTP**, and As_2O_3-**Cu-Ag-PTP** treated groups had significantly reduced expression levels of Beclin1 and LC3 (by approximately 67% and 49% for As_2O_3-**Cu-Zn-PTP**; 62% and 44% for As_2O_3-**Cu-Ni-PTP**; 15% and 21% for As_2O_3-**Cu-Co-PTP**; and 19% and 13% for As_2O_3-**Cu-Ag-PTP, respectively**), particularly in the group treated with As_2O_3-**Cu-Zn-PTP** and As_2O_3-**Cu-Ni-PTP**, compared to the arsenic group ($p < 0.05$) (Table 4, Fig. 7A and B). This outcome aligns with the results of Saha *et al.*,[73] who observed that supplementing with genistein reduced the autophagic mechanism of death by downregulating the expression of autophagy regulatory molecules (Beclin1, PINK1, Parkin 1, LCIIIB) in both age groups that were arsenic

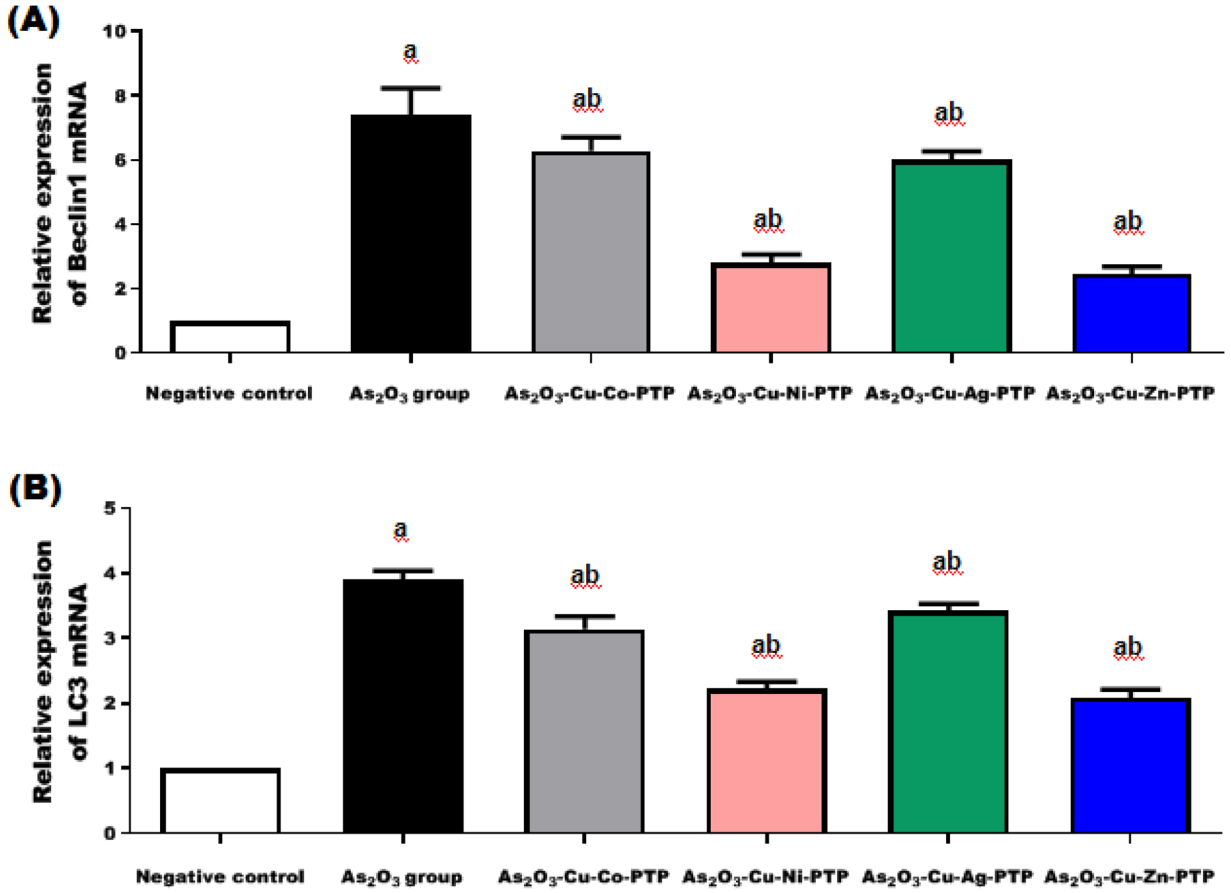

Fig. 7 (A and B) Investigation of the autophagy-related genes Beclin1 and LC3 in the studied groups using real-time polymerase chain reaction. One-way ANOVA was used to analyze the data, and then the Tukey–Kramer multiple comparison test was used. Every value ($n = 6$) was shown as mean ± SEM. [a] $p < 0.05$ in comparison to the control group; [b] $p < 0.05$ in comparison to the group that was treated with As_2O_3.

intoxicated. Meanwhile, Rahaman *et al.*[67] found that, in comparison to cells treated just to As^{3+} (10 μM), co-exposure with curcumin (2.5 μM) and As^{3+} (10 μM) significantly down-regulated the expressions of ULK1 and LC3-II. All of the results showed that the metal complexes As_2O_3-**Cu-Zn-PTP** and As_2O_3-**Cu-Ni-PTP** effectively decreased the toxicity that arsenic trioxide caused in the lungs by suppressing genes associated with autophagy (Beclin1 and LC3) and apoptosis (BAX and ERK), indicating that these metal complexes may have a therapeutic role in the treatment of lung injury disease.

6.4. Docking and MD simulation

The **PTP** complexes were docked with the crystal structure of the autoinhibited dimer of pro-apoptotic BAX(I) (PDBID: 4S0O)[35] and HUMAN BCL-2, ISOFORM 1 (PDBID: 1G5M),[36] which is displayed in Fig. 8 and Table 5. Firstly, the docking of Cu-bimetallic complexes with PDBID: 4s0O showed binding affinity with Cu–Ni complex with the strongest binding energy −12.87 kcal mol^{-1}, then the Cu–Zn complex with −12.43, and the Cu–Ag complex −12.03, while the Cu–Co complex showed the least binding with −11.53 kcal mol^{-1}. Furthermore, the inhibitory constant K_i showed Cu–Ni complex with the lowest with 9.76 μM, indicating to strongest inhibition, while the Cu–Co complex showed the highest K_i with 10.45 μM, with weak inhibition. Also, the Cu–Zn showed the longest 1.85, 1.98 Å, and the shortest of Cu–Co with 1.25 Å. **Cu-Ag-PTP** shows two close bond distances (1.1, 1.15 Å), possibly due to bidentate coordination. The binding amino acids showed that **Cu-Ni-PTP** binds mostly to hydrophobic residues (Leu 47, Val 50) and a key catalytic residue (Asp 48), **Cu-Co-PTP** interacts with charged residues (Asp 142, Glu 146, Arg 145), suggesting electrostatic stabilization, **Cu-Zn-PTP** binds near aromatic residues (Tyr 164, Phe 176), possibly π-interactions, and **Cu-Ag-PTP** interacts with Glu 17 (charged) and Met 20 (sulfur-containing), indicating potential metal–thiolate bonding. The van der Waals + H-bond + desolvation energy showed that **Cu-Ag-PTP** and **Cu-Ni-PTP** have the strongest contributions (∼−22.65 kcal mol^{-1}), and their electrostatic energy showed **Cu-Ag-PTP** has the strongest electrostatic stabilization (−12.97 kcal mol^{-1}) and the internal energy of **Cu-Zn-PTP** has the most favorable unbound energy (−21.87 kcal mol^{-1}). The RMSD of the **Cu-Ni-PTP** has the lowest RMSD (0.87 Å), indicating the most stable docking pose, while the **Cu-Co-PTP** has the highest RMSD (1.03 Å), suggesting slight conformational flexibility. So we **Cu-Ni-PTP** (strongest binding, lowest Ki, most stable pose) and **Cu-Ag-PTP** shows strong electrostatic interactions, possibly due to Ag^{+}'s high polarizability.

Fig. 8 Docking and dynamics of the Cu-bimetallic **PTP** with PDBID: 4s0O and 1G5M; respectively.

Cu–Ni & Cu–Zn rely heavily on hydrophobic/van der Waals packing (high vdW terms). The molecular dynamics of these bimetallics showed the RMSD of the Ni with less RMSD, while

Table 5 Docking simulation analysis of the interaction of MOLP-1 and MOLP-1-AgNPs with PDBID: 4s0O and 1G5M, respectively

Compound	Binding energy (BE)	Binding distance	Inhibitory constant, K_i (μM)	Binding amino acids	vdW + H bond + desolv energy	Electrostatic energy	Total internal, unbound energy	RMSD
PDBID: 4s0O								
Cu-Ni-PTP	−12.87	1.54	**9.76**	Leu 47, Ala 24, Asp 48, Val 50, Gly 138, Arg 134	**−22.65**	−13.86	−21.76 (hydrophobic + ionic dominance)	0.87
Cu-Co-PTP	−11.53	1.25	10.45	Asp142, Arg 145, Gly 138, Glu 146, Arg 134	−21.65	−11.87	−19.76 (weaker electrostatics)	1.03
Cu-Zn-PTP	−12.43	1.85, 1.98	**9.90**	Tyr 164, Val 173, Ser 163, Phe 176	**−22.23**	−12.39	−21.87 (balanced forces)	0.90
Cu-Ag-PTP	−12.03	1.1, 1.15	10.05	Glu 17, Met 20	−22.24	−12.97	−20.98 (strong electrostatics (Ag^+ polarizability))	0.96
PDBID: 1G5M								
Cu-Ni-PTP	−10.84	1.23	**7.36**	Asp 10, Ser 49, Arg 6, Gly 5, Thr 7, Glu 13, Glu 45	−23.98	−9.87	−19.34	0.98 (shows good stability with minor backbone drift)
Cu-Co-PTP	−9.42	2.44, 2.97	8.20	Gln 118, Arg 129, Glu 136	−20.54	−7.00	−17.45	1.12 (indicates slightly more flexibility or local unfolding)
Cu-Zn-PTP	−10.23		7.88		−23.65	−9.00	−18.78	1.02 (most stable with tighter folding)
Cu-Ag-PTP	−10.02	1.87	8.06	Phe 124, Arg 127, Gly 128	−22.43	−8.34	−18.00	1.09 (medium flexibility)

the Co highest and the Co showed fluctuations. The RMSF showed Asp 48 (**Cu-Ni-PTP**) or Glu 17/Met 20 (**Cu-Ag-PTP**) exhibit restricted motion (indicating strong binding), and the metal–ligand distance dynamics showed **Cu-Ni-PTP** (1.54 Å) *vs.* **Cu-Zn-PTP** (1.85/1.98 Å) for deviations, Ag–S (Met 20) bond stability in **Cu-Ag-PTP** (short bond in docking). The hydrogen bond of Ser 163 (**Cu-Zn-PTP**) H-bond persistence, and energy contributions (MM-PBSA/GBSA) showed **Cu-Ni-PTP** ≈ **Cu-Zn-PTP** > **Cu-Ag-PTP** > **Cu-Co-PTP**. The heatmap allow residue by residue of structural flexibility through Cu complex which showed Ni rigid targets, Ag showed most flexibility which is good in dynamic binding, **Cu-Co-PTP** and **Cu-Zn-PTP** balance stability and flexibility (possibly catalytic candidates).[75–77]

The docking with PDBID:1 G5M with metal–**PTP** binding affinity of the **Cu-Ni-PTP** has the strongest binding energy (−10.84 kcal mol^{-1}), **Cu-Co-PTP** has the weakest (−9.42 kcal mol^{-1}), while the **Cu-Zn-PTP** and **Cu-Ag-PTP** are intermediate (−10.23 and −10.02 kcal mol^{-1}, respectively). Their inhibitory constant **Cu-Ni-PTP** has the lowest K_i (7.36 μM), meaning it is the strongest inhibitor. **Cu-Co-PTP** has the highest K_i (8.20 μM), making it the weakest inhibitor's-Ni-**PTP** has the shortest binding distance (1.23 Å), suggesting tight binding; **Cu-Co-PTP** has longer distances (2.44, 2.97 Å), possibly explaining weaker binding's-Ni-**PTP** interacts with Asp 10, Ser 49, Arg 6, Gly 5, Thr 7, Glu 13, Glu 45, **Cu-Co-PTP** binds Gln 118, Arg 129, Glu 136, and **Cu-Ag-PTP** interacts with Phe 124, Arg 127, Gly 128. All complexes have RMSD < 1.2 Å, indicating relatively stable docking poses. The dynamics of all complexes with RMSD below ∼2.1 Å, **Cu-Zn-PTP** has the lowest average RMSD, making it a candidate for the most structurally rigid complex, and **Cu-Co-PTP** shows the highest flexibility, which may correlate with a looser metal-binding pocket or dynamic behavior. The heat map showed the RMSD of **Cu-Ni-PTP** and **Cu-Zn-PTP** show low, uniform RMSD (blue/green), indicating stable binding over time. **Cu-Co-PTP** exhibits high RMSD fluctuations (yellow/red), suggesting structural instability and possible metal dissociation. **Cu-Ag-PTP** has intermediate stability, with minor deviations. The RMSF of metal-binding residues (*e.g.*, Asp 10, Arg 6, Glu 13) shows low RMSF (dark colors), confirming their rigid, well-defined coordination in **Cu-Ni-PTP** and **Cu-Zn-PTP**, **Cu-Co-PTP** displays higher flexibility (bright spots) near binding sites, explaining its weaker inhibitory activity. The binding interaction of **Cu-Ni-PTP** has strong, persistent contacts (red) with key residues (Arg 6, Glu 13, Asp 10), justifying its highest binding affinity (ΔG = −10.84 kcal mol^{-1}), **Cu-Co-PTP** shows sporadic interactions (yellow/white), correlating with its poor inhibition (K_i = 8.20 μM), and **Cu-Zn-PTP** and **Cu-Ag-PTP** exhibit moderate contact frequencies, consistent with their intermediate binding energies.[78–80]

6.5. Molecular dynamics validation and binding energy analysis

To supplement the docking results, molecular dynamics (MD) simulations were conducted for 100 ns at 300 K with the GROMACS package using the AMBER99SB-ILDN force field. The simulation featured explicit solvation using TIP3P water molecules, as well as metal-specific parameters.[77,81–85] The trajectory analysis quantitatively confirmed the structural stability and binding affinity of the Cu-M-PTP complexes, where M = Co, Ni, Zn or Ag.

6.5.1. RMSD and structural stability. Backbone root mean square deviation (RMSD) values were calculated for each of the protein–ligand complexes. All systems equilibrated within the first 10–15 ns and remained stable throughout the simulation, with the RMSD consistently fluctuating below 2 Å. **Cu-Ni-PTP** complexes exhibited the lowest mean RMSD of 1.05 ± 0.12 Å, indicating a more rigid structure and converged trajectories in their binding modes. **Cu-Zn-PTP** exhibited a slightly higher RMSD (1.24 ± 0.18 Å) while still exhibiting stable dynamics. **Cu-Ag-PTP** exhibited RMSD below 1.36 Å with transient fluctuations occurring around 35 ns, likely a result of flexible surface loops. **Cu-Co-PTP** exhibited the highest deviation with an RMSD of 1.73 ± 0.22 Å, indicating a complex that was less stabilized relative to the others.

6.5.2. RMSF and residue flexibility. Analysis of root-mean-square fluctuation (RMSF) showed that for residues involved with metal binding (*i.e.*, Asp48, Glu17, Ser49, and Arg6), the atomic displacement was relatively modest (<1.5 Å) across all metal complexes. In contrast, the regions moving through the loops of the structure (*i.e.*, residues 120–150) exhibited greater fluctuations (∼2.3 Å) as expected for flexing solvent-exposed domains. Finally, the **Cu-Ni-PTP** and **Cu-Zn-PTP** complexes showed the lowest RMSF, suggestive of a more compact and stable bound conformation than other complexes.

6.5.3. Potential energy and stability. Total potential energy curves generated from the gmx energy module presented well-converged, flat profiles with low drift. The average potential energy ranked from lowest to highest was as follows: **Cu-Ni-PTP:** −6.42 × 10^5 kJ mol^{-1}, **Cu-Zn-PTP:** −6.38 × 10^5 kJ mol^{-1}, **Cu-Ag-PTP:** −6.33 × 10^5 kJ mol^{-1} and **Cu-Co-PTP:** −6.21 × 10^5 kJ mol^{-1}. The low standard deviations (<1.5 × 10^3 kJ mol^{-1}) for each system suggest energetic stability and reasonable convergence for the MD trajectories.

Table 6 MM/PBSA binding-free-energy components (kcal mol^{-1}) for Cu-M-PTP complexes over the final 50 ns of simulation

Complex	ΔE_vdW (kcal mol^{-1})	ΔE_elec (kcal mol^{-1})	ΔG_polar (kcal mol^{-1})	ΔG_nonpolar (kcal mol^{-1})	ΔG_bind (kcal mol^{-1})
Cu-Ni-PTP	−47.28 ± 1.3	−21.64 ± 0.8	23.17 ± 1.2	−5.26 ± 0.4	−51.01 ± 1.9
Cu-Zn-PTP	−45.63 ± 1.5	−20.11 ± 1.0	21.95 ± 1.4	−4.87 ± 0.5	−48.66 ± 2.0
Cu-Ag-PTP	−42.55 ± 1.6	−19.32 ± 0.9	22.43 ± 1.5	−4.76 ± 0.3	−44.20 ± 2.1
Cu-Co-PTP	−40.17 ± 1.8	−17.24 ± 1.1	24.18 ± 1.7	−4.23 ± 0.4	−37.46 ± 2.5

6.6. MM/PBSA binding free energy evaluation

The MM/PBSA method was utilized to calculate binding free energies (ΔG_bind) derived from snapshots of the last 50 ns of each molecular dynamics simulation. Further decomposition of the energy terms revealed that van der Waals and electrostatic interactions were the predominant favorable contributions to the formation of the complex, while polar solvation energies acted as a small penalty against binding. This is consistent with the general trend observed in stable protein–ligand complexes described in the literature.[86,87]

Table 6 contains a summary of the energy components for each Cu-M-PTP complex, showing the balance of enthalpic favorability against solvation penalties.

The ranking of binding free energy observed in the results of the binding studies: Cu–Ni > Cu–Zn > Cu–Ag > Cu–Co correlates accurately with the docking data, supporting the general conclusion that Ni- and Zn-complexes were the ones that formed the most favorable and stable interactions with the BAX and BCL-2 protein targets. The consistently low and highly negative ΔG_bind values (<−45 kcal mol^{-1}) indicate spontaneous binding and strong thermodynamic stability of the complexes, particularly **Cu-Ni-PTP** and **Cu-Zn-PTP**, further reinforcing the evidence of strong therapeutic candidates from these complexes.[88,89]

7. Conclusion

All four new heterodimetallic complexes based on the thiazole–phthalimide ligand (**PTP**), interacted with Cu(II) to complex with Co(II), Ni(II), Zn(II), and Ag(I), were synthesized and characterized in solid and solution state by FT-IR, UV-Vis, AS, magnetic susceptibility, conductivity, and thermal analysis methods. The structural elucidation data indicate tetradentate coordination with O_2N_2 donor atoms. Overall, these findings demonstrate the detrimental effects of arsenic toxicity on pulmonary architecture and suggest the involvement of oxidative stress, apoptosis, and autophagy mechanisms in the development of the disease. In addition, the present study highlighted the therapeutic efficacy of a novel phthalimide analog to treat arsenic-induced lung injury in rat. The phthalimide analog increased GSH activity and reduced MDA level. Moreover, the analog suppressed APAF-1 protein abundance in lung tissues. Furthermore, the analog revealed anti-apoptotic properties by enhancing and suppressing BCL2 levels. In addition, these phthalimide analogs effectively mitigated the injurious effects of arsenic in lung tissue by suppressing apoptotic genes (BAX and ERK) and autophagy genes (Beclin1 and LC3). Among all the phthalimide analogs, As_2O_3-**Cu-Zn-PTP** and As_2O_3-**Cu-Ni-PTP** demonstrated the greatest activity in all biochemical parameters and decreased all genes studied; however, this class of compounds has significant application potential against arsenic *in vivo* model. Additionally, experimental data were supported by molecular docking and molecular dynamics simulations showing stable energetically favorable interactions between the tested complexes and pro-and anti-apoptotic proteins (BAX and BCL-2). These results suggest the synthesized thiazole–phthalimide heterobimetallic complexes exhibit antioxidant, anti-apoptotic, and cytoprotective properties to mitigate arsenic-induced lung injury. Of the complexes tested, the Cu–Zn–phthalimide (**Cu-Zn-PTP**) exhibited the greatest stability, binding affinity, and biological efficacy, making it promising for therapeutic candidates to treat oxidative stress-mediated and heavy metal-induced lung disorders. Future studies will extend this work to understand the mechanistic role of the free ligand (**PTP**) and the homo-bimetallic analogues to determine if the observed metal metal synergism holds. Overall, phthalimide analogs can ameliorate arsenic-induced lung injury by regulating oxidative stress, inflammation, apoptosis, and autophagy.

Ethical approval

This study was approved by the Medical Research Ethics Committee of the National Research Centre, Egypt (Approval no. 11410625).

Conflicts of interest

There are no conficts to declare.

Data availability

The data supporting this study's findings are available from the corresponding author, Asmaa M. Fahim, on request.

Supplementary information (SI) is available. See DOI: https://doi.org/10.1039/d5ra07055d.

References

1 M. G. Rizk, *et al.*, Novel metal complexes of N1,N2-bis(4-phenylthiazol-2-yl)phthalamide: Synthesis, spectroscopic, thermal and kinetic investigations, molecular modeling, computational calculations, anti-breast cancer studies, *J. Mol. Struct.*, 2023, **1277**, 134816, DOI: 10.1016/j.molstruc.2022.134816.

2 P.-P. Yang, *et al.*, Syntheses, Crystal Structures, and Magnetic Properties of a Family of Tetra- and Octanuclear Mixed-Valent Manganese Clusters, *Eur. J. Inorg. Chem.*, 2013, **2013**(30), 5288–5296, DOI: 10.1002/ejic.201300582.

3 S. J. Lee and W. Lin, Chiral Metallocycles: Rational Synthesis and Novel Applications, *Acc. Chem. Res.*, 2008, **41**(4), 521–537, DOI: 10.1021/ar700216n.

4 M. Schmittel and K. Mahata, Multicomponent Assembly of Heterometallic Isosceles Triangles, *Inorg. Chem.*, 2009, **48**(3), 822–824, DOI: 10.1021/ic8021084.

5 G. H. Elsayed and A. M. Fahim, Studying the impact of chitosan salicylaldehyde/schiff base/CuFe2O4 in PC3 cells via theoretical studies and inhibition of PI3K/AKT/mTOR signalling, *Sci. Rep.*, 2025, **15**(1), 4129, DOI: 10.1038/s41598-025-86096-7.

6 T. Gupta, *et al.*, Surface-Confined Heterometallic Molecular Dyads: Merging the Optical and Electronic Properties of Fe, Ru, and Os Terpyridyl Complexes, *Adv. Funct. Mater.*, 2013, **23**(34), 4227–4235, DOI: 10.1002/adfm.201203404.

7 H. Sepehrpour, M. L. Saha and P. J. Stang, Fe–Pt Twisted Heterometallic Bicyclic Supramolecules via Multicomponent Self-Assembly, *J. Am. Chem. Soc.*, 2017, **139**(7), 2553–2556, DOI: 10.1021/jacs.6b11860.

8 A. M. Fahim, S. A. Abdelhamid and T. A. Hameed, Antimicrobial, antioxidant activities and ADME studies of novel BaSnO3 sulphone cellulose with docking simulation, *J. Mol. Struct.*, 2025, **1325**, 140945, DOI: 10.1016/j.molstruc.2024.140945.

9 K. Ahmed, H. Elhennawy and M. Elkashouti, Microwave assists the synthesis of pyridone azo dyes and their application in polyester printing, *Res. J. Chem. Sci.*, 2012, **2231**, 606X.

10 N. H. Mahmoud and A. M. Fahim, The Effect of Anion, Steric Factors on the Catalytic Activity of Hydrogen Peroxide, Biological Activities, Docking, and DFT Calculations of Novel Mixed Ligand of Copper Complexes, *Appl. Organomet. Chem.*, 2025, **39**(6), e70220, DOI: 10.1002/aoc.70220.

11 W. Linert, N. Mahmoud and A. Abu-Hussen, Solvatochromism of copper (II) complexes derived from trifluoroacetylacetone and dinitrogen ligands, *Arch. Chem. Res.*, 2019, **1**(4), 1.

12 A. Kamal, *et al.*, Naphthalimide derivatives with therapeutic characteristics: a patent review, *Expert Opin. Ther. Pat.*, 2013, **23**(3), 299–317, DOI: 10.1517/13543776.2013.746313.

13 M. N. Ahmed, *et al.*, Supramolecular assembly involving weak hydrogen bonds, anti-parallel π···π stacking and O···C tetrel bonding interactions and LOX studies in a 1H-pyrazol-1-yl)thiazole-4-carboxylate derivative: An experimental and theoretical study, *J. Mol. Struct.*, 2024, **1296**, 136908, DOI: 10.1016/j.molstruc.2023.136908.

14 A. A. A. Emara, *et al.*, Spectroscopic, solvent influence and thermal studies of ternary copper(II) complexes of diester and dinitrogen base ligands, *Spectrochim. Acta, Part A*, 2010, **77**(3), 594–604, DOI: 10.1016/j.saa.2010.06.012.

15 Y. F. Cheng, *et al.*,Heavy Metals Toxicity: Mechanism, Health Effects, and Therapeutic Interventions., *MedComm*, 2025, **6**(9), e70241, DOI: 10.1002/mco2.70241.

16 K. L. Cooper, *et al.*, Particulate arsenic trioxide induces higher DNA damage and reactive oxygen species than soluble arsenite in lung epithelial cells., *Toxicol. Appl. Pharmacol., Suppl.*, 2022, **457**, 116320, DOI: 10.1016/j.taap.2022.116320.

17 S. Fang, *et al.*, *Arsenic trioxide induces macrophage autophagy and atheroprotection by regulating ROS-dependent TFEB nuclear translocation and AKT/mTOR pathway.*, *Cell Death Dis.*, 2021, **12**(1), 88, DOI: 10.1038/s41419-020-03357-1.

18 N. Mizushima, *et al.*, The ATG conjugation systems in autophagy., *Curr. Opin. Cell Biol.*, 2020, **63**, 1–10, DOI: 10.1016/j.ceb.2019.12.001.

19 M. M. Ommati, *et al.*, Arsenic-induced autophagic alterations and mitochondrial impairments in HPG-S axis of mature male mice offspring (F1-generation): A persistent toxicity study., *Toxicol. Lett.*, 2020, **326**, 83–98, DOI: 10.1016/j.toxlet.2020.02.013.

20 A. A. Abou-Hussein, N. H. Mahmoud and W. Linert, Syntheses, solvatochromism, and antimicrobial activities of new binuclear copper(II) mixed-ligand complexes in a ternary system with β-diketones and diamine ligands, *J. Coord. Chem.*, 2011, **64**(15), 2592–2605, DOI: 10.1080/00958972.2011.602402.

21 M. V. Varghese, Attenuation of arsenic trioxide induced cardiotoxicity through flaxseed oil in experimental rats, *Redox Rep.*, 2017, **22**(6), 346–352, DOI: 10.1080/13510002.2017.1289313.

22 B. El-Aarag, *et al.*, New phthalimide analog ameliorates CCl4 induced hepatic injury in mice via reducing ROS formation, inflammation, and apoptosis. toxicity study, *Saudi J. Biol. Sci.*, 2021, **28**(11), 6384–6395, DOI: 10.1016/j.sjbs.2021.07.014.

23 L. F. Van Pelt, Ketamine and Xylazine for Surgical Anesthesia in Rats, *J. Am. Vet. Med. Assoc.*, 1977, **171**(9), 842–844, DOI: 10.2460/javma.1977.171.09.842.

24 D. A. Sorg and B. Buckner, A Simple Method of Obtaining Venous Blood from Small Laboratory Animals., *Proc. Soc. Exp. Biol. Med.*, 1964, **115**(4), 1131–1132, DOI: 10.3181/00379727-115-29134.

25 H. M. Carleton, *et al.*, *Carleton's Histological technique*, Oxford University Press, NY, USA, 4th edn, 1967, pp. 279–280, DOI: 10.1016/j.sjbs.2021.07.014.

26 K. J. Livak and T. D. Schmittgen, Analysis of Relative Gene Expression Data Using Real-Time Quantitative PCR and the 2−ΔΔCT Method, *Methods*, 2001, **25**(4), 402–408, DOI: 10.1006/meth.2001.1262.

27 N. M. Abdelazeem, *et al.*, Design, synthesis, docking studies and biological evaluation of novel benzochromenopyrimidines via silica sulfuric acid catalyzed reaction on apoptosis in human cancer cells, *Polycyclic Aromat. Compd.*, 2023, **43**(9), 8569–8592.

28 N. A. Ali, *et al.*, Chia Seed (Salvia hispanica) Attenuates Chemically Induced Lung Carcinomas in Rats through Suppression of Proliferation and Angiogenesis, *Pharmaceuticals*, 2024, **17**(9), 1129.

29 G. Albasher, Ameliorative Effect of Beta vulgaris Root Extract on Chlorpyrifos-Induced Oxidative Stress, Inflammation and Liver Injury in Rats, *Biomolecules*, 2019, **9**(7), 261.

30 Y. Jiang, *et al.*, Influence of miR-1 on Nerve Cell Apoptosis in Rats with Cerebral Stroke via Regulating ERK Signaling Pathway, *BioMed Res. Int.*, 2021, **2021**(1), 9988534.

31 J. Zhang, *et al.*, Fluoride-Induced Autophagy via the Regulation of Phosphorylation of Mammalian Targets of Rapamycin in Mice Leydig Cells, *J. Agric. Food Chem.*, 2017, **65**(40), 8966–8976, DOI: 10.1021/acs.jafc.7b03822.

32 S. Vilar, G. Cozza and S. Moro, Medicinal chemistry and the molecular operating environment (MOE): application of QSAR and molecular docking to drug discovery, *Curr. Top. Med. Chem.*, 2008, **8**(18), 1555–1572.

33 B. L. Jejurikar and S. H. Rohane, *Drug Designing in Discovery Studio*, 2021.

34 D. Van Der Spoel, *et al.*, GROMACS: fast, flexible, and free, *J. Comput. Chem.*, 2005, **26**(16), 1701–1718.

35 T. P. Garner, *et al.*, An Autoinhibited Dimeric Form of BAX Regulates the BAX Activation Pathway, *Mol. Cell*, 2016, **63**(3), 485–497, DOI: 10.1016/j.molcel.2016.06.010.
36 A. M. Petros, *et al.*, Solution structure of the antiapoptotic protein bcl-2, *Proc. Natl. Acad. Sci. U. S. A.*, 2001, **98**(6), 3012–3017, DOI: 10.1073/pnas.041619798.
37 A. M. Fahim, Structure-based drug design; Computational strategies in drug discovery; Antihypertensive agents; Antiviral drugs; Molecular docking; QSAR; Pharmacological insights, *Comput. Biol. Chem.*, 2026, **120**, 108663, DOI: 10.1016/j.compbiolchem.2025.108663.
38 M. A. Ayoub, A. M. Fahim and H. S. Magar, Novel Schiff base Cu(ii) and Au(iii) complexes: spectroscopic, computational, and electrochemical insights for H2O2 sensor applications, *RSC Adv.*, 2025, **15**(49), 41447–41470, DOI: 10.1039/D5RA06669G.
39 M. Szymańska, *et al.*, Thiophene-benzothiazole dyad ligand and its Ag(I) complex – Synthesis, characterization, interactions with DNA and BSA, *J. Mol. Liq.*, 2020, **319**, 114182, DOI: 10.1016/j.molliq.2020.114182.
40 C. A. Téllez Soto, *et al.*, Surface enhancement Raman scattering of tautomeric thiobarbituric acid. Natural bond orbitals and B3LYP/6-311+G (d,p) assignments of the Fourier Infrared and Fourier Raman Spectra, *Spectrochim. Acta, Part A*, 2013, **114**, 475–485, DOI: 10.1016/j.saa.2013.05.035.
41 S. L. Stefan, *et al.*, Determination of some lanthanide ions by conductometric and spectrophotometric measurements of their hydrazo-5-pyrazolone complexes, *Microchem. J.*, 1987, **35**(1), 51–65, DOI: 10.1016/0026-265X(87)90199-8.
42 W. H. Mahmoud, R. G. Deghadi and G. G. Mohamed, Preparation, geometric structure, molecular docking thermal and spectroscopic characterization of novel Schiff base ligand and its metal chelates, *J. Therm. Anal. Calorim.*, 2017, **127**(3), 2149–2171, DOI: 10.1007/s10973-016-5826-7.
43 N. H. Mahmoud, *et al.*, Spectroscopic studies, DFT calculations, cytotoxicity activity, and docking stimulation of novel metal complexes of Schiff base ligand of isonicotinohydrazide derivative, *Appl. Organomet. Chem.*, 2022, **36**(7), e6697, DOI: 10.1002/aoc.6697.
44 E. Yousif, *et al.*, Metal complexes of Schiff base: Preparation, characterization and antibacterial activity, *Arabian J. Chem.*, 2017, **10**, S1639–S1644, DOI: 10.1016/j.arabjc.2013.06.006.
45 K. Nakamoto, *Infrared and Raman Spectra of Inorganic and Coordination Compounds, Part A: Theory and Applications in Inorganic Chemistry*, John Wiley & Sons/Wiley-Interscience, New Jersey/Hoboken, NJ, USA, 6th edn, 2009.
46 G. H. Elsayed, *et al.*, Investigation of anticancer and anti-inflammatory efficacies of novel metal complexes: Spectroscopic and thermal characterization, computational investigation, and docking simulation, *Inorg. Chem. Commun.*, 2025, **182**, 115427, DOI: 10.1016/j.inoche.2025.115427.
47 A. M. Fahim, H. S. Magar and N. H. Mahmoud, Synthesis, antimicrobial, antitumor activity, docking simulation, theoretical studies, and electrochemical analysis of novel Cd(II), Co(II), Cu(II), and Fe(III) complexes containing barbituric moiety, *Appl. Organomet. Chem.*, 2023, **37**(4), e7023, DOI: 10.1002/aoc.7023.
48 M. Wei, *et al.*, Alleviation of Arsenic-Induced Pulmonary Oxidative Damage by GSPE as Shown during In vivo and In vitro Experiments, *Biol. Trace Elem. Res.*, 2018, **183**(1), 80–91, DOI: 10.1007/s12011-017-1111-2.
49 M. Muthumani and S. Miltonprabu, Arsenic induced oxidative stress and its possible reversal by chelation therapy, *Res. Rev.: J. Toxicol.*, 2012, **408**(2), 16–37.
50 M. Ashrafuzzaman, *et al.*, Bioactive Mixed Ligand Metal Complexes Of Cu(II), Ni(II), And Zn(II) Ions: Synthesis, Characterization, Antimicrobial And Antioxidant Properties, *J. Chil. Chem. Soc.*, 2021, **66**, 5295–5299.
51 N. Sridevi and D. Madheswari, Synthesis, characterization, and biological evaluation of Schiff base ligand and their metal complexes: implications for coordination chemistry and biomedical applications, *Polyhedron*, 2025, **282**, 117796, DOI: 10.1016/j.poly.2025.117796.
52 A. Sharma, *et al.*, Quercetin protects against chronic arsenic trioxide–induced oxidative stress in rat brain, *Neurosci. Lett.*, 2014, **558**, 99–104.
53 T. Tasci, *et al.* N-acetylcysteine attenuates sodium arsenite-induced oxidative stress and apoptosis in embryonic fibroblast cells, *Toxicol. Res.*, 2024, **13**(4), tfae128, DOI: 10.1093/toxres/tfae128.
54 C. Perkins, R. Dagda, J. Angermann, *et al.*, Arsenic induces apoptosis of multidrug-resistant human myeloid leukemia cells that express Bcr-Abl or overexpress MDR, MRP, Bcl-2, or Bcl-x(L), *Blood*, 2000, **95**(3), 1014–1022.
55 W.-S. Juan, *et al.*, Arsenic compounds activate MAPK and inhibit Akt pathways to induce apoptosis in MA-10 mouse Leydig tumor cells, *Cancer Med.*, 2023, **12**(3), 3260–3275, DOI: 10.1002/cam4.5068.
56 A. S. Noman, *et al.*, Arsenic-induced Histological Alterations in Various Organs of Mice, *J. Cytol. Histol.*, 2015, **6**(3), DOI: 10.4172/2157-7099.1000323.
57 S. Mingxing, *et al.*, Acute toxicity of intratracheal arsenic trioxide instillation in rat lungs, *J. Appl. Toxicol.*, 2019, **39**(11), 1578–1585, DOI: 10.1002/jat.3841.
58 P. Chen, *et al.*, Copper complexes as potential therapeutic agents: Antioxidant, anticancer, and anti-inflammatory activities, *Coord. Chem. Rev.*, 2020, **408**, 213177, DOI: 10.1016/j.ccr.2020.213177.
59 M. Korani, *et al.*, Acute and subacute dermal toxicity of nanosilver in guinea pig: Histopathological, hematological, and biochemical findings, *Toxicol. Ind. Health*, 2015, **31**(5), 447–454, DOI: 10.1177/0748233712472528.
60 S. Shafique, *et al.*, Protective effect of zinc against arsenic-induced oxidative stress and DNA damage in rat lung, *Biol. Trace Elem. Res.*, 2019, **190**(2), 403–411, DOI: 10.1007/s12011.
61 C. C. Yen, *et al.*, Inorganic arsenic causes cell apoptosis in mouse cerebrum through an oxidative stress-regulated signaling pathway, *Arch. Toxicol.*, 2011, **85**(6), 565–575, DOI: 10.1007/s00204-011-0709-y.
62 A. E. Siddique, *et al.*, Association between chronic arsenic exposure and the characteristic features of asthma,

Chemosphere, 2020, **246**, 125790, DOI: 10.1016/j.chemosphere.2019.125790.

63 A. Olfati and E. Tvrda, Riboflavin recovery of spermatogenic dysfunction via a dual inhibition of oxidative changes and regulation of the PINK1-mediated pathway in arsenic-injured rat model, *Physiol. Res.*, 2021, **70**(4), 591–603, DOI: 10.33549/physiolres.934658.

64 P. Nouri and A. Olfati, The Effects of Maternal Exposure Riboflavin to Prevent Uterus Arsenic Damage in Offspring Rats, *J. Hum., Environ., Health Promot.*, 2021, **7**(4), 182–188, DOI: 10.52547/jhehp.7.4.182.

65 N. Medda, S. K. De and S. Maiti, Different mechanisms of arsenic related signaling in cellular proliferation, apoptosis and neo-plastic transformation, *Ecotoxicol. Environ. Saf.*, 2021, **208**, 111752, DOI: 10.1016/j.ecoenv.2020.111752.

66 G. Zhong, *et al.*, Arsenic or/and antimony induced mitophagy and apoptosis associated with metabolic abnormalities and oxidative stress in the liver of mice, *Sci. Total Environ.*, 2021, **777**, 146082.

67 M. S. Rahaman, *et al.*, Curcumin alleviates arsenic-induced toxicity in PC12 cells via modulating autophagy/apoptosis, *Environ. Health Prev. Med.*, 2020, **200**, 110756.

68 S. Tripathi, *et al.*, Nuclear factor erythroid 2-related factor 2 (Nrf2) signaling in heavy metals-induced oxidative stress, *Heliyon*, 2024, **10**(18), e37545.

69 R. Liu, *et al.*, Effect of Beclin-1 gene silencing on autophagy and apoptosis of the prostatic hyperplasia epithelial cells, *Clinics*, 2022, **77**, 100076.

70 C. Ren, *et al.*, Paradoxical effects of arsenic in the lungs. Environmental Health and Preventive Medicine, *Environ. Health Prev. Med.*, 2021, **26**(1), 80.

71 Y. Qi, *et al.*, Autophagy Inhibition by Sustained Overproduction of IL6 Contributes to Arsenic Carcinogenesis, *Cancer Res.*, 2014, **74**(14), 3740–3752, DOI: 10.1158/0008-5472.can-13-3182.

72 J. Mao, *et al.*, Arsenic Inhibits Proliferation and Induces Autophagy of Tumor Cells in Pleural Effusion of Patients with Non-Small Cell Lung Cancer Expressing EGFR with or without Mutations via PI3K/AKT/mTOR Pathway, *Biomedicines*, 2023, **11**(6), 1721.

73 S. Saha, *et al.*, Ameliorative role of genistein against age-dependent chronic arsenic toxicity in murine brains via the regulation of oxidative stress and inflammatory signaling cascades, *J. Nutr. Biochem.*, 2018, **55**, 26–40, DOI: 10.1016/j.jnutbio.2017.11.010.

74 R. Kang, *et al.*, The Beclin 1 network regulates autophagy and apoptosis, *Cell Death Differ.*, 2011, **18**(4), 571–580, DOI: 10.1038/cdd.2010.191.

75 A. Aboelnaga, *et al.*, Novel bis pyrimidine-pyrazolone and pyridinyl-4, 5-dihydropyrimido [2, 1 [1]-c, 1, 2, 4] triazepine utilized ultrasonic energy, anti-proliferative activity, docking simulation, and theoretical investigation, *J. Mol. Struct.*, 2023, **1294**, 136517.

76 H. Bayrak, *et al.*, Synthesis, In Silico Studies, Antimicrobial, Antioxidant Activities, Docking Simulation, and Computational Analysis of Novel Acrylamide Derivatives, *Russ. J. Gen. Chem.*, 2024, **94**(8), 2044–2060, DOI: 10.1134/S1070363224080188.

77 A. Chaima, A. M. Fahim and L. Jouffrey, Crystal description, vibrational and DFT investigation of a new organic-inorganic compound based on Sn(IV): Bis(3.5-dimethylanilinium) hexachloridostannate (IV) dihydrate (C8H11N)2[SnCl6]·2H2O, *J. Mol. Struct.*, 2026, **1353**, 144522, DOI: 10.1016/j.molstruc.2025.144522.

78 F. N. El-Shall, A. M. Fahim and S. Dacrory, Making a new bromo-containing cellulosic dye with antibacterial properties for use on various fabrics using computational research, *Sci. Rep.*, 2023, **13**(1), 10066, DOI: 10.1038/s41598-023-36688-y.

79 A. M. Fahim, Exploring novel benzene sulfonamide derivatives: Synthesis, ADME studies, anti-proliferative activity, docking simulation, and emphasizing theoretical investigations, *J. Indian Chem. Soc.*, 2024, **101**(8), 101211, DOI: 10.1016/j.jics.2024.101211.

80 A. M. Fahim, Anti-proliferative activity, molecular docking study of novel synthesized ethoxyphenylbenzene sulfonamide with computational calculations, *J. Mol. Struct.*, 2023, **1277**, 134871, DOI: 10.1016/j.molstruc.2022.134871.

81 A. M. Fahim and M. G. Elbanna, A novel ruthenium(VI) benzylidene carbene complex: Synthesis, crystal structure, hirshfeld surface, electrochemical behavior, and DFT insights, *J. Mol. Struct.*, 2026, **1351**, 144381, DOI: 10.1016/j.molstruc.2025.144381.

82 M. Hashem, A. M. Fahim and F. Helaly, Designing a green poly (β-amino ester) for the delivery of nicotinamide drugs with biological activities and conducting a DFT investigation, *RSC Adv.*, 2024, **14**(8), 5499–5513.

83 A. Heidari, A. M. Fahim and M. Heidari Majd, Elucidating CT-DNA refolding and antitumor efficacy of novel phendione-Pd(II) complexes: A comprehensive computational and experimental study, *Int. J. Biol. Macromol.*, 2025, **327**, 147305, DOI: 10.1016/j.ijbiomac.2025.147305.

84 A. I. Khodair, *et al.*, Synthesis, DFT investigation, molecular docking analysis, ADMET studies, and biological evaluation of a novel series of imidazolidinone derivatives as potential antimicrobial agents, *J. Mol. Struct.*, 2025, **1322**, 140586, DOI: 10.1016/j.molstruc.2024.140586.

85 M. S. Hashem, *et al.*, Alginate sulfonamide hydrogel beads for 5-fluorouracil delivery: antitumor activity, cytotoxicity assessment, and theoretical investigation, *Int. J. Biol. Macromol.*, 2024, **282**, 136573, DOI: 10.1016/j.ijbiomac.2024.136573.

86 G. Abdel-Maksoud, A. M. Fahim and R. A. Sobh, Preliminary evaluation of green terpolymer of nano poly (methyl methacrylate/dimethylaminoethyl methacrylate/acrylamide) for the consolidation of bone artifacts, *J. Cult. Herit.*, 2025, **73**, 139–149, DOI: 10.1016/j.culher.2025.03.002.

87 A. M. Fahim and K. M. Abas, Properties and computational insights of catalysts based on amide linked polymer for photo-Fenton remediation of Rhodamine B dye, *Sci. Rep.*, 2025, **15**(1), 30566, DOI: 10.1038/s41598-025-13192-z.

88 J. Makhlouf, *et al.*, Synthesis-Controlled Polymorphism in bis(Benzylammonium) Tetrathiocyanatocobaltate(II): Distinct Crystal Packing (C2/c vs. P21) Dictates Band Gap Energy and Superior Antimicrobial Performance with computational investigation, *J. Mol. Struct.*, 2025, 144809, DOI: 10.1016/j.molstruc.2025.144809.

89 G. H. Elsayed and A. M. Fahim, Synthesis, theoretical investigation, and anti-proliferative assessment of novel fused heterocyclic cellulosic derivatives in colorectal Caco-2 cells via suppressing the IL6/STAT3 pathway, *J. Mol. Struct.*, 2025, **1347**, 143045, DOI: 10.1016/j.molstruc.2025.143045.